Destratification and Restratification of the Spring Surface Boundary Layer in a Subtropical Front

ERIC KUNZE,[a] JOHN B. MICKETT,[b] AND JAMES B. GIRTON[b]

[a] *NorthWest Research Associates, Redmond, Washington*
[b] *Applied Physics Laboratory, University of Washington, Seattle, Washington*

(Manuscript received 11 January 2021, in final form 26 April 2021)

ABSTRACT: Destratification and restratification of a ~50-m-thick surface boundary layer in the North Pacific Subtropical Front are examined during 24–31 March 2017 in the wake of a storm using a ~5-km array of 23 chi-augmented EM-APEX profiling floats (u, v, T, S, χ_T), as well as towyo and ADCP ship surveys, shipboard air-sea surface fluxes, and parameterized shortwave penetrative radiation. During the first four days, nocturnal destabilizing buoyancy fluxes mixed the surface layer over almost its full depth every night followed by restratification to $N \sim 2 \times 10^{-3}$ rad s^{-1} during daylight. Starting on 28 March, nocturnal destabilizing buoyancy fluxes weakened because weakening winds reduced latent heat flux. Shallow mixing and stratified transition layers formed above ~20-m depth. A remnant layer in the lower part of the surface layer was insulated from destabilizing surface forcing. Penetrative radiation, turbulent buoyancy fluxes, and horizontal buoyancy advection all contribute to its restratification, closing the budget to within measurement uncertainties. Buoyancy advective restratification (slumping) plays a minor role. Before 28 March, measured advective restratification $\int(u_z b_x + v_z b_y)\,dt$ is confined to daytime; is often destratifying; and is much stronger than predictions of geostrophic adjustment, mixed-layer eddy instability, and Ekman buoyancy flux because of storm-forced inertial shear. Starting on 28 March, while small, the subinertial envelope of measured buoyancy advective restratification in the remnant layer proceeds as predicted by mixed-layer eddy parameterizations.

KEYWORDS: Fronts; Mass fluxes/transport; Oceanic mixed layer; Surface layer

1. Introduction

The ocean surface boundary layer (SL) is characterized by weak stratification so that it is often referred to as a mixed layer—though it is usually not fully mixed (e.g., Taylor and Ferrari 2011; Johnson et al. 2020a)—overlying a more strongly stratified pycnocline. This layer is subject to direct forcing by penetrative radiation, atmospheric surface heating and cooling, evaporation and precipitation, and wind stress that control its thickness, SST, and stratification (Price et al. 1986; Stramma et al. 1986; Price et al. 1987; Kantha and Clayson 1994; Large et al. 1994). These in turn influence air–sea gas exchange (Longhurst and Harrison 1989; Longhurst et al. 1995; Sabine et al. 2004), primary productivity, timing of the spring bloom, and carbon sequestration (Sverdrup 1953; Smetacek et al. 1978; Townsend et al. 1994; Huisman et al. 1999; McGillicuddy et al. 2007; Behrenfeld 2010; Taylor and Ferrari 2011; Mahadevan et al. 2012; Swart et al. 2015), as well as feedback to the atmospheric boundary layer (Jochum 2009; Belcher et al. 2012).

Historically, the surface layer has been treated in 1D (Kraus and Turner 1967; Niiler and Kraus 1977; Price et al. 1986, 1987; Kantha and Clayson 1994; Large et al. 1994). However, recent work suggests that lateral buoyancy gradients associated with submesoscale surface-layer fronts can modulate the surface boundary layer's stratification and timing of the spring phytoplankton bloom (Mahadevan et al. 2010; Fox-Kemper et al. 2011; Mahadevan et al. 2012; Swart et al. 2015; Johnson et al. 2016, 2020a,b). Based on measured air–sea fluxes and water column turbulent fluxes in an eastern North Pacific front, Brainerd and Gregg (1993a) reported diurnal restratification exceeding 1D predictions by 40%, and suggested that horizontal processes might be responsible. Motivated by these observations, Tandon and Garrett (1994) modeled slumping of unbounded lateral buoyancy gradients at rest in the wake of vertical homogenization of the surface layer by nocturnal cooling or a storm, finding restratification by geostrophic adjustment of $(b_h^2/f^2)[1-\cos(ft)]$ where b_h is the horizontal buoyancy-gradient magnitude and f the Coriolis frequency. Following establishment of a thermal-wind balance on a time scale $\sim O(f^{-1})$, submesoscale mixed-layer eddy (MLE) instabilities, on time scales $\sim O(1\text{–}10f^{-1})$ depending on the strength of lateral buoyancy gradients, have been argued to further extract available potential energy (APE) from the horizontal buoyancy gradients to continue restratification of the surface layer (Haine and Marshall 1998; Boccaletti et al. 2007; Fox-Kemper et al. 2008; Fox-Kemper and Ferrari 2008). MLE instability has been found to persist under moderate winds in numerical simulations (Mahadevan et al. 2010; Capet et al. 2008) though it is necessarily reset by strong destabilizing air–sea forcing (e.g., Haney et al. 2012). The role of lateral effects will depend on the presence and strength of density fronts,

Denotes content that is immediately available upon publication as open access.

Corresponding author: Eric Kunze, kunze@nwra.com

DOI: 10.1175/JPO-D-21-0003.1

which occupy $\sim O(10\%)$ of the surface area of the ocean boundary layer (Rudnick and Ferrari 1999; Johnson et al. 2012), imbalanced vertical shears and the strength of 1D processes. They are thought to be particularly important for the timing of the spring bloom during transition when mixed layers are deep enough to be outside the range of shortwave penetrative radiation.

Recent ocean process studies have rarely exceeded 40 h or 1.5 inertial periods (e.g., Hosegood et al. 2008; Johnson et al. 2020a) so arguably are dominated by inertial shear which might not produce irreversible restratification. Mahadevan et al. (2012) reported evidence for buoyancy advective restratification (slumping) in the subpolar North Atlantic, equivalent to an ageostrophic velocity difference that must have persisted over 10 days and 200 km exceeding 10 cm s^{-1} across the 250-m-thick surface layer, prior to dominance by spring shortwave penetrative radiation.

Destratification processes include radiative cooling, evaporation and evaporative (latent) cooling, turbulent mixing, wind stress, sensible cooling, downfront winds, and shear advection with time scales ranging from hours to weeks. Restratification processes include surface heating and shortwave penetrative radiation, precipitation, upfront winds, and shear advection—for example, by geostrophic adjustment and mixed-layer eddy instability, also with time scales ranging from hours to weeks. While 1D contributions from air–sea buoyancy fluxes, shortwave penetrative radiation, wind stress, and turbulent buoyancy fluxes have been synthesized into 1D surface-layer models (Price et al. 1986; Kantha and Clayson 1994; Large et al. 1994), 2D and 3D effects due to the vertical shearing of horizontal buoyancy gradients by wind-driven flows (Ekman buoyancy flux), geostrophic adjustment and MLE instability have largely been studied in isolation with a notable exception of numerical simulations of the decay of a hurricane cold wake by Haney et al. (2012). The multiple processes and time scales are nonlinearly intertwined so that they can only be realistically examined in isolation for special cases where only one or two processes dominate.

This paper describes the stratification budget in the North Pacific Subtropical Front using 4D measurements collected during March 2017. Section 2 describes the measurements, section 3 the overall evolution of the surface-layer stratification and section 4 nocturnal destratification during the first half of the week-long time series. Section 5 compares measured daytime restratification in the surface layer both prior to 28 March, and over 72 h in an isolated remnant layer that forms after 28 March, to contributions from penetrative radiation, turbulent buoyancy flux and horizontal advection, closing the stratification budget (with transient exceptions). Section 6 isolates the role of horizontal advection and compares the observations with parameterizations based on geostrophic adjustment, MLE, and Ekman buoyancy flux (EBF). Results are summarized and discussed in sections 7 and 8. Because turbulent buoyancy fluxes can only be reliably inferred from our measurements of temperature microstructure χ_T in stratified waters below the influence of surface-forced convection, this paper will focus on surface-layer evolution and dynamics in the daylight restratifying surface layer and restratification in the remnant layer.

2. Measurements

With the primary goal of measuring the contribution of horizontal advection to surface-layer restratification, sampling was conducted at three sites in the North Pacific Subtropical Front NNE of Hawaii (Roden 1975, 1981; Van Woert 1982; Cushman-Roisin 1984; Hosegood et al. 2006, 2008, 2013; Shcherbina et al. 2009, 2010) during March 2017. The sites were selected based on daily satellite SST and AVISO SSH maps, as well as the ship's throughflow CTD measurements to ensure sharp in situ horizontal density gradients on $\sim O(5)$ km lateral scales. Site 1 at 26°N, 146°W was sampled during 7–12 March, site 2 at 30°N, 146°W during 15–21 March, and site 3 at 35°N, 140°W during 24–31 March. At each site, a drifting air–sea flux buoy and arrays of 9, 16, and 23 EM-APEX profiling floats (Sanford et al. 2005; Carlson et al. 2006), respectively, were deployed with initial float separations of $\sim O(1)$ km. The floats were programmed to profile continuously and synchronously in the upper 100–150 m of the water column. All floats measure horizontal velocity (u, v), temperature T and salinity S with ~3-m vertical and ~1-h temporal resolutions. Relative velocity uncertainties in each profile are ~0.5 cm s^{-1} while velocities made absolute with surface GPS fixes have larger uncertainties of ~2 cm s^{-1}. Some of the floats were instrumented with microscale FP07 temperature sensors to estimate turbulent thermal-variance dissipation rates χ_T on 1-m scales. The EM float array will be treated as a semi-Lagrangian profile time series, as might be measured by a drifting chain, able to measure ~5-km lateral buoyancy gradients (b_x, b_y) as a function of time and depth using least squares lateral plane fits over the array (see section 5). The Lagrangian assumption is justified by lateral displacements of the surface layer relative to the array (inferred from the velocity profiles) being a factor of 2 smaller than array dimensions.

While the EM float array followed depth-averaged water motion, the ship conducted 6–8-km box surveys around it with the towyo platform Shallow-Water Integrated Mapping System (SWIMS) (Klymak and Gregg 2001; Hosegood et al. 2006, 2008, 2013; Shcherbina et al. 2009, 2010) profiling temperature, salinity, pressure, optical backscatter, oxygen, and fluorescence every ~0.5 km. Each box survey took ~5 h to complete. Additional shipboard survey measurements included a 300-kHz ADCP and shipboard air–sea fluxes.

The reduced time–space aliasing of the EM float arrays afforded by its rapid synchronous sampling proved more suitable for inferring horizontal buoyancy gradients at the ~1-h temporal resolution needed to perform surface-layer stratification budgets. While ADCP shears were inertial and closely resembled those from the EM floats, inclusion of SWIMS density measurements in horizontal buoyancy-gradient inferences produced large fluctuations in (b_x, b_y) on the time scale of the box surveys, and including these data for buoyancy advective restratification $\int(u_z b_x + v_z b_y)\,dt$ overestimated measured restratification. In-depth analysis of shipboard SWIMS and ADCP surveys at all three sites will be reported elsewhere.

Restratification in the upper 50 m is often dominated by shortwave penetrative radiation buoyancy flux $J_b(z)$ (Brainerd and Gregg 1993b; Hosegood et al. 2008). Since profiling radiometer measurements were not made, it is critical to minimize penetrative radiation errors to ensure parameterized values are not attributed to other processes. The double-exponential model

$$Q_s(z) = Q_s(0^-)\left[A_1 \exp\left(\frac{z}{B_1}\right) + (1 - A_1)\exp\left(\frac{z}{B_2}\right)\right],$$

(Paulson and Simpson 1977), where z is negative downward, $Q_s(0^-) = (1 - \text{albedo})Q_s(0^+)$ is the downwelling shortwave radiation just below the sea surface and an invariant albedo = 0.06, was selected over more recent models that account for solar zenith angle, cloudiness, and chlorophyll concentrations (e.g., Ohlmann and Siegel 2000; Ohlmann 2003) after comparison with 15 photosynthetically active radiation (PAR) profiles collected during the cruise, as well as with SeaWiFS Profiling Multichannel Radiometer (SPMR) measurements with a similar chlorophyll profile collected in the same region and time of year as part of the 2004 Mixed-Layer Restratification Experiment (ML04; Hosegood et al. 2008). PAR-derived profiles use a depth-dependent conversion factor (Morel and Smith 1974). Since the focus here is below 10-m depth, the deep decay length scale $B_2 = 23.62 \pm 1.30$ m and amplitude $A_2 = 1 - A_1 = 0.36 \pm 0.06$ were derived from exponential fits to seven ML04 transmission profiles over 10–65-m depth ($R^2 > 0.98$); these values are close to standard deep decay length scale and amplitude values for expected Jerlov IA conditions ($B_2 = 20$ m and $A_2 = 0.38$). The shallow decay length scale $B_1 = 0.6$ m is also based on Jerlov water-type IA. In contrast, the Ohlmann and Siegel (2000) and Ohlmann (2003) models overestimate PAR-derived $Q_s(z)$ decay scales over 10–65 m. Downwelling shortwave radiation just above the surface $Q_s(0^+)$ was measured with a shipboard Remote Measurements and Research Company Radiometer Analog-to-Digital (RAD) Interface with an Eppley PSP shortwave radiometer. Nighttime offsets to the shortwave radiation were corrected with a daily linear fit between the infrared (PIR) and shortwave (PSP) measurements. After correction, absolute errors in $Q_s(0^+)$ are less than $\pm 10\,\mathrm{W\,m^{-2}}$ (MacWhorter and Weller 1991). Downwelling shortwave radiation $Q_s(0^+)$ was set to zero between evening and morning twilight. Bad data during the day were filled in with linear interpolation. Buoy shortwave measurements were compromised by improper placement of sensors on its mast but were largely consistent with the shipboard measurements and helped identify errors. Shipboard data on clear days were also verified with a clear-sky shortwave model (Ineichen and Perez 2002). Absolute uncertainties in $Q_s(z)$ are less than $\pm 2\,\mathrm{W\,m^{-2}}$ below 20 m. Accounting for uncertainties in the deep amplitude A_2 and decay length scale B_2, and assuming a daily-averaged $Q_s(0^-)$ of $200\,\mathrm{W\,m^{-2}}$, the mean and uncertainty for the penetrative radiation contribution to restratification $\partial^2 J_b(z)/\partial z^2$ are $(2.3 \pm 0.6) \times 10^{-6}\,\mathrm{s^{-2}\,day^{-1}}$ at 20-m depth and $(1.0 \pm 0.2) \times 10^{-6}\,\mathrm{s^{-2}\,day^{-1}}$ at 40-m depth.

At all three sites, typical March mixed-layer thickness are $\sim O(100)$ m based on examination of a previous decade of Argo

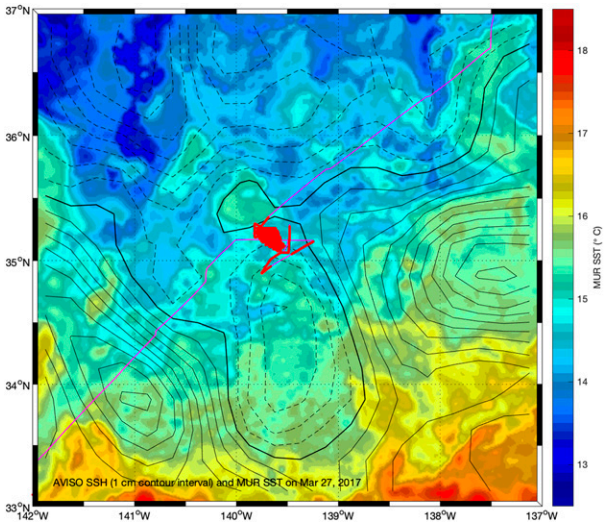

FIG. 1. Satellite SST (color) and AVISO SSH (1-cm contours) on 27 Mar along with the site 3 ship track over 24–31 Mar on the north-northeast corner of a cyclonic eddy (red). Evolving convoluted meso/submesoscale fronts are present throughout the domain.

float profiles. This contrasts with our in situ measurements—despite the North Pacific marine heatwave known as the Blob having ended 6 months earlier. At site 1, while there was evidence of a relict mixed layer extending to ~100-m depth, it had buoyancy frequencies $N = (0.4\text{–}1.0) \times 10^{-2}\,\mathrm{s^{-1}}$. At site 2, a 20-m-thick well-mixed layer was present but average buoyancy frequency over 100 m was $(0.5\text{–}1.0) \times 10^{-2}\,\mathrm{s^{-1}}$. Only at site 3 was a ~60-m thick well-mixed nocturnal layer present. With vertical resolution for velocity of ~5 m and surface-wave contamination above 15-m depth, surface-layer thicknesses were too thin at sites 1 and 2 to examine horizontal advective restratification (slumping) so attention is restricted here to site 3 (inertial period ~21 h) where a convoluted field of evolving submesoscale surface fronts is present (Fig. 1).

Following deployment, the 23 site-3 EM profiling floats drifted to the northwest at $\sim 3\,\mathrm{cm\,s^{-1}}$, spreading from a ~4-km circle with typical float separations of 0.5–1 km to a zonally elongated ellipse with a ~15-km major axis, 8-km minor axis and float separations of 2–4 km. The array also underwent spatially coherent ~2 km ($20\,\mathrm{cm\,s^{-1}}$) clockwise-rotary-in-time inertial/diurnal circles (Fig. 2) that decayed over the week-long deployment. The dimension of the array is comparable to surface-layer Rossby length scale NH/f of approximately 3 km, which is expected to control the width of surface-layer buoyancy fronts (Fox-Kemper et al. 2011).

3. Evolution of the surface-layer stratification

The surface layer is defined as the ~50–70-m-thick boundary layer overlying the top of the permanent pycnocline based on the depth of maximum stratification below 50-m depth, $N \sim 8 \times 10^{-3}\,\mathrm{rad\,s^{-1}}$ (Fig. 3). The top of the permanent pycnocline exhibits super- and subinertial heaving. The surface boundary layer underwent a rich range of variability as surface forcing

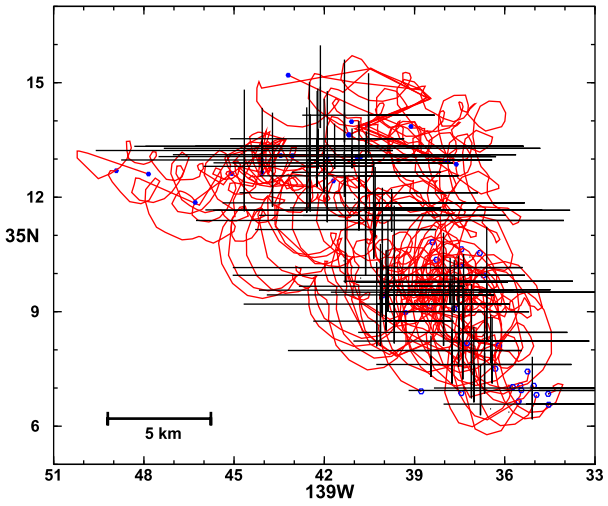

FIG. 2. EM float tracks (red), along with 4-h binned array mean positions and extents (black crosses), at site 3 during 24–31 Mar 2017. Open blue circles mark the beginning of each float's track and solid dots its end. The tracks reveal a superposition of coherent decaying clockwise-rotary-in-time inertial circles, a drift to the northwest at ~3 cm s^{-1}, and spreading from a ~4-km diameter circle on 24 Mar to an ellipse with a zonal major axis of ~15 km and meridional minor axis of ~8 km by 31 Mar.

changed in the wake of a storm on 23 March. Before 28 March, it describes a diurnal cycle of a nocturnally destratifying mixing layer (ML) with $N^2 \leq 0$ over almost its full thickness, followed by daytime restratification to $N \sim 2 \times 10^{-3}$ rad s^{-1}. Destratification lags with depth as turbulence forced by surface cooling J_{b0} and wind stress $\boldsymbol{\tau}_w$ erodes stratification downward. In contrast, restratification appears almost instantly with morning shortwave penetrative radiation $J_b(z)$. Starting on 28 March, the SL encompasses a shoaling ML and stratified transition layer (TL) above ~20-m depth, both influenced by weakening surface-forced buoyancy fluxes and wind stress, overlying a restratifying remnant layer (RL) insulated from destabilizing surface forcing. On 28 March, the stratified transition layer erodes downward and is eradicated by nocturnal cooling. But after 30 March, nocturnal destratifying buoyancy fluxes are too weak to erase the TL which developed maximum stratification $N \sim 8 \times 10^{-3}$ rad s^{-1} between ~10- and 20-m depth. The ML is then confined above ~5 m so cannot be resolved. The isolated ~22–46-m remnant layer weakly restratifies to $\sim 4 \times 10^{-3}$ rad s^{-1} during the remainder of the time series. Thus, the week-long record shifts from a winter (or storm) to spring (or calm) diurnal cycle.

Bulk 5–55-m depth-averaged variables provide a broad-brush overview of surface-layer evolution (Fig. 4). Surface-layer densities are $\langle \sigma_\theta \rangle_z = 25.18$–$25.19$ on the night of 24 March, decreasing to 25.14 during the day of 25 March, then spreading to fill this density range with some densification that might be due to upward incursions of the pycnocline into the averaging depths (Fig. 4a). The surface layer is most susceptible to shear instability in the first half of the record (Fig. 4b). Bulk buoyancy frequency $N = b_z^{1/2}$ and vertical shear magnitude $|\mathbf{V}_z| = (u_z^2 + v_z^2)^{1/2}$ track each other closely before 28 March (Fig. 4b), e.g., both N and shear decrease through the nights of 25 and 26 March, with values lying between 10^{-4} and 6×10^{-3} rad s^{-1}. Shear magnitude is intermittently below N, mostly

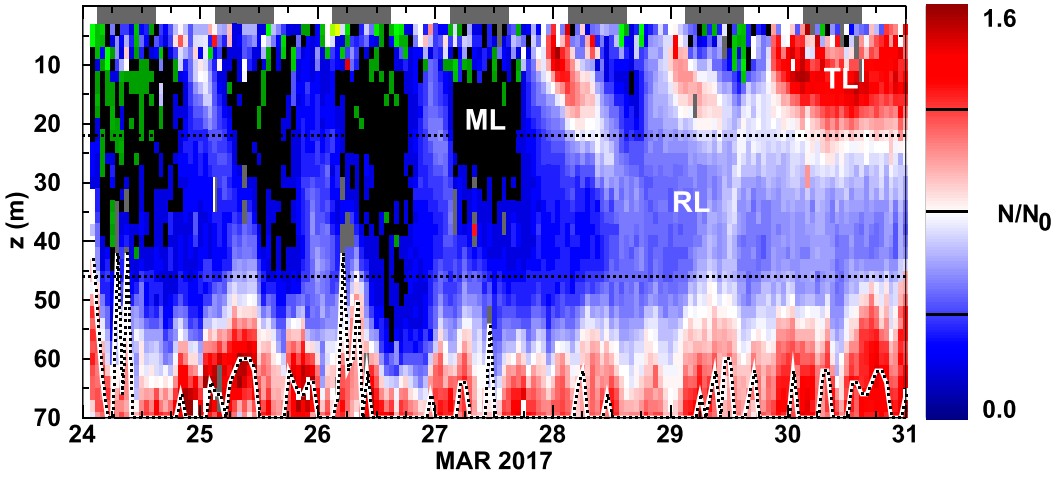

FIG. 3. Profile time series of normalized buoyancy frequency N/N_0 where $N_0 = 5 \times 10^{-3}$ rad s^{-1}. Plotted values are averages across the EM float array in 2-m and 1-h bins. Black denotes no stratification ($N^2 = 0$) and green unstable stratification ($N^2 < 0$). Gray bars just below the upper axis mark local nighttime. The black dotted curve near the lower axis marks the highest stratification in the underlying permanent pycnocline, which is taken to be the base of the surface boundary layer (SL) and exhibits both super- and subinertial heaving. Horizontal black dotted lines at 22- and 46-m depth nominally straddle the remnant layer (RL) that starts on 28 Mar. Deep mixing layers (ML) form at night before 28 Mar but shoal above 20 m in the latter half of the time series. A highly stratified transition layer (TL) appears between 5- and 20-m depth starting on 28 Mar that is no longer eroded away at night starting on 30 Mar.

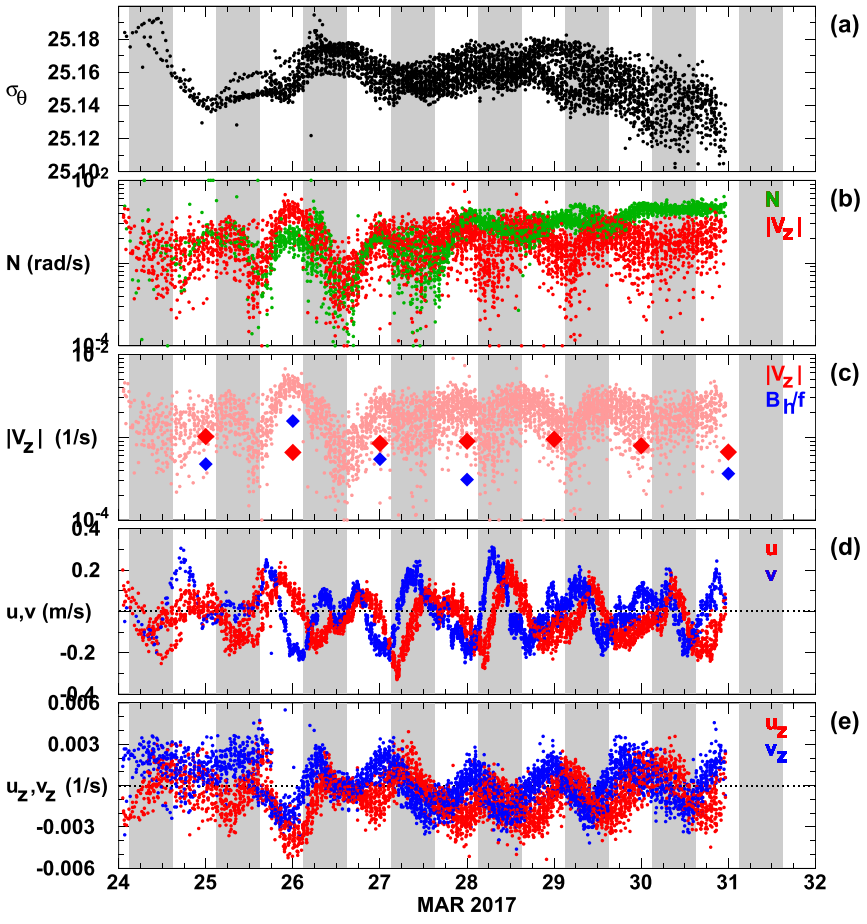

FIG. 4. Bulk EM float time series of 5–55-m depth-average instantaneous surface-layer (a) density σ_θ, (b) buoyancy frequency N (green) and vertical shear magnitude $|\mathbf{V}_z|$ (red), (c) vertical shear magnitude $|\mathbf{V}_z|$ (pink) along with inertially averaged vertical shear (red diamonds) and normalized horizontal buoyancy gradient $|B_h|/f$ (blue diamonds), (d) zonal velocity u (red) and meridional velocity v (blue), and (e) zonal shear u_z (red) and meridional shear v_z (blue). Data are plotted for each profile of each float except the inertial averages in (c), which are also averages across the array. Surface-layer velocities in (d) show a mix of inertial/diurnal and semidiurnal motions while vertical shears in (e) are initially scattered then become inertial/diurnal modulated by nocturnal destratification starting on 26 Mar. Buoyancy frequency N and vertical shear $|\mathbf{V}_z|$ in (b) closely track each other though sometimes one falls much below the other at night. Inertially averaged vertical shear and normalized horizontal buoyancy gradient in (c) should be identical for thermal wind.

during night, while bulk buoyancy frequency N only falls below shear during the nights of 26 and 27 March. After 26 March, diurnal variability in buoyancy frequency N diminishes while vertical shear continues to exhibit a minimum at the beginning of nightfall with inertial/diurnal periodicity. By 30 March, $N \sim 5 \times 10^{-3}\,\mathrm{rad\,s^{-1}}$ and $|\mathbf{V}_z| \sim (1\text{–}3) \times 10^{-3}\,\mathrm{rad\,s^{-1}}$ with little diurnal variability. Histograms of both variables (not shown) have tails toward low values $\sim 10^{-4}\,\mathrm{rad\,s^{-1}}$ with a mode in N at (3–4) $\times 10^{-3}\,\mathrm{rad\,s^{-1}}$, mode in $|\mathbf{V}_z| \sim 2 \times 10^{-3}\,\mathrm{rad\,s^{-1}}$ (gradient Froude number $\delta_N = |\mathbf{V}_z|/N \sim 0.6\text{–}1$), and mode in reduced shear $|\mathbf{V}_z| - 2N$ at $-5 \times 10^{-3}\,\mathrm{rad\,s^{-1}}$, that is, stable. Tandon and Garrett's (1994) geostrophic adjustment model, which neglects other sources of shear such as wind-forcing or the underlying internal-wave field, trends to $\delta_N = 1$ in its subinertial approximation and $\delta_N = 1.4$ when inertial oscillations are allowed.

Daily- and array-averaged normalized horizontal buoyancy-gradient magnitudes $|\mathbf{B}_h|/f$ based on linear least squares plane fits over the array (see section 5) differ from daily-averaged $|\mathbf{V}_z| \sim 10^{-3}\,\mathrm{s^{-1}}$ (Fig. 4c) by a factor of 2, with $|\mathbf{B}_h|/f < |\mathbf{V}_z|$ in most cases. Therefore, surface-layer subinertial shear and buoyancy gradients are *not* in thermal-wind balance. Bulk subinertial horizontal buoyancy gradients imply isopycnal slopes $s = |\mathbf{B}_h|/B_z \sim 0.1f/N$ where $\sim O(f/N)$ is the maximum stable slope for thermal wind.

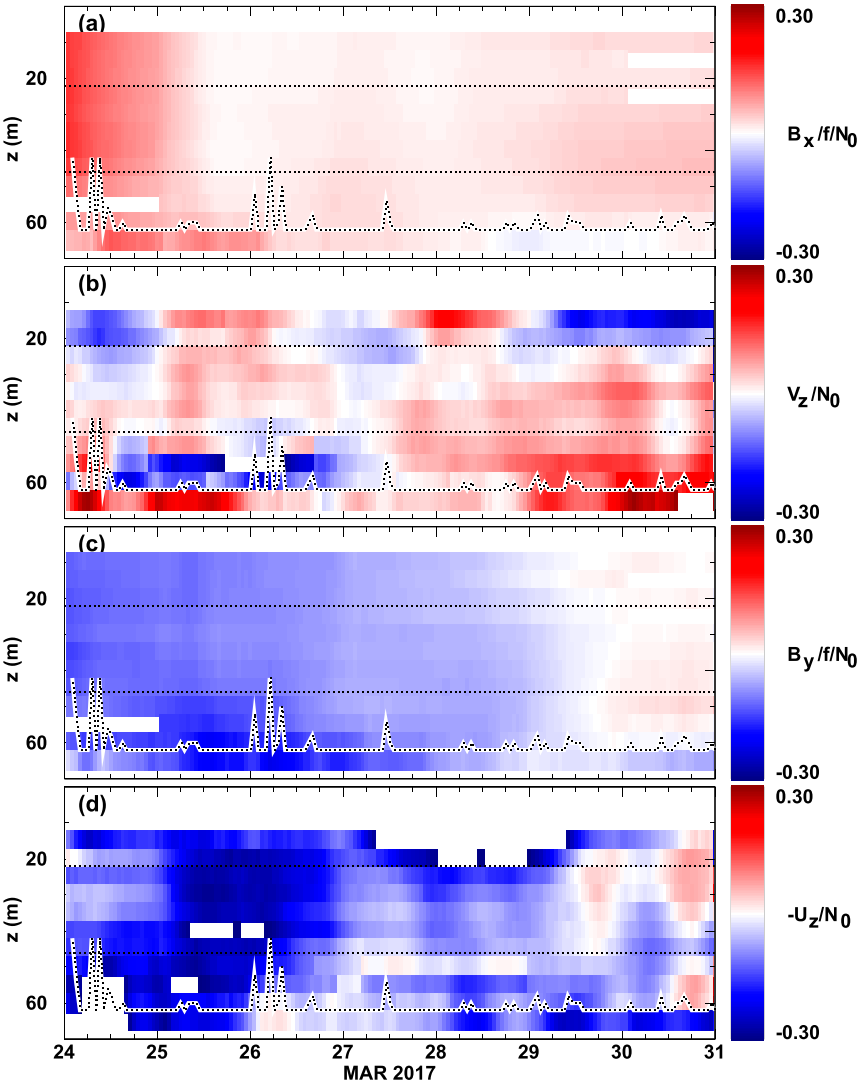

FIG. 5. Profile time series of normalized subinertial horizontal buoyancy gradients (a) $B_x/f/N_0$ and (c) $B_y/f/N_0$ and vertical shears (b) V_z/N_0 and (d) $-U_z/N_0$ smoothed over four inertial periods, where $N_0 = 5 \times 10^{-3}$ rad s^{-1} and $f = 0.8 \times 10^{-4}$ rad s^{-1}. As in Fig. 4c, these are not in thermal-wind balance. Vertical shear exhibits shorter time and depth scales than lateral buoyancy gradients. Dotted curves mark the base of the SL, and dotted horizontal lines at 22- and 46-m depth straddle the RL.

Daily-averaged gradient Froude number $\delta_N = |\mathbf{V}_z|/N$ diminishes from ~1 on 25 March to ~0.1 on 29–31 March so that the maximum mixed-layer instability growth rate

$$\sigma_{\mathrm{mx}} = f\sqrt{\frac{5}{54}}\frac{\delta_N}{\sqrt{1+\delta_N^2}} \qquad (1)$$

(Stone 1970) decreases from $0.25f$ to $0.1f$, that is, substantially subinertial. Growth rates would be smaller if calculated from horizontal buoyancy gradients assuming thermal wind. Conditions are not met for symmetric instability (e.g., Thomas et al. 2013).

Bulk surface-layer velocities of 10–20 cm s^{-1} are clockwise-rotary-in-time (v leading u) with a mix of low-mode inertial/diurnal and semidiurnal time scales (Fig. 4d) while surface-layer vertical shears are predominantly inertial/diurnal (Fig. 4e).

Subinertial vertical shears (U_z, V_z) and horizontal buoyancy gradients (B_x, B_y) smoothed over four inertial periods exhibit strikingly different vertical structure, temporal behavior, and signs (Fig. 5), underscoring that they are not in thermal-wind balance; this behavior is robust to smoothing over 1–4 inertial periods. Subinertial vertical shear has shorter time and vertical scales than horizontal buoyancy gradients which are almost depth-independent. Unbalanced (ageostrophic) conditions are necessary for lateral buoyancy advective restratification as explored in sections 5 and 6 since $U_zB_x + V_zB_y = U_zV_z/f - V_zU_z/f = 0$ for thermal wind.

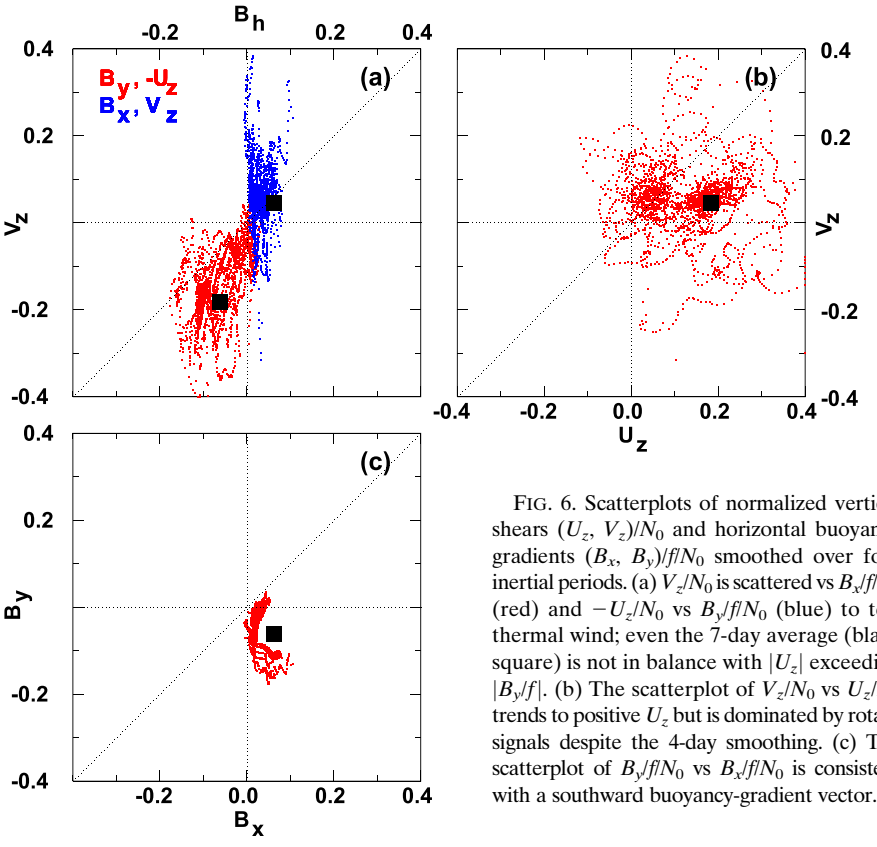

FIG. 6. Scatterplots of normalized vertical shears $(U_z, V_z)/N_0$ and horizontal buoyancy gradients $(B_x, B_y)/f/N_0$ smoothed over four inertial periods. (a) V_z/N_0 is scattered vs $B_x/f/N_0$ (red) and $-U_z/N_0$ vs $B_y/f/N_0$ (blue) to test thermal wind; even the 7-day average (black square) is not in balance with $|U_z|$ exceeding $|B_y/f|$. (b) The scatterplot of V_z/N_0 vs U_z/N_0 trends to positive U_z but is dominated by rotary signals despite the 4-day smoothing. (c) The scatterplot of $B_y/f/N_0$ vs $B_x/f/N_0$ is consistent with a southward buoyancy-gradient vector.

Subinertial imbalance in the surface layer can arise from geostrophic adjustment (Tandon and Garrett 1994), MLE instability (Haine and Marshall 1998; Boccaletti et al. 2007; Fox-Kemper et al. 2008; Fox-Kemper and Ferrari 2008; Mahadevan et al. 2010; Fox-Kemper et al. 2011; Haney et al. 2012), wind-driven (Ekman) shear (Thomas and Lee 2005; Haney et al. 2012), turbulent momentum-flux modification of geostrophic adjustment (Dauhajre and McWilliams 2018; Johnson et al. 2020b) or nonstationary near-inertial oscillations (Hosegood et al. 2013; Johnson et al. 2020a).

Scatterplots of subinertial vertical shears and horizontal buoyancy gradient smoothed over four inertial periods hint at surface-intensified eastward flow and a southward buoyancy-gradient vector in thermal-wind balance (Fig. 6) but the 7-day average is out of balance with $|U_z|$ exceeding $|B_y/f|$ and unbalanced clockwise-rotary-in-time variability in the vertical shear dominates on shorter subinertial time scales (Fig. 6b). Subinertial shear has rms magnitudes a factor of 5 smaller than unsmoothed shear (Figs. 4b,e). Its rotary variability is robust to smoothing over 1–4 inertial periods. Free surface-intensified evanescent subinertial solutions are allowed with $\omega^2 = f^2 - N^2k^2/|m^2| < f^2$ if vertical wavenumbers m are imaginary, that is, corresponding to exponential decay with depth. However, smoothed Pollard and Millard (1970) wind-forced slab model simulations with a time-varying depth of momentum penetration suggest that this rotary shear signal might be an artifact of averaging time variability in the wind-forced response (not shown).

4. Nocturnal destratification

Destratification largely arises from nocturnal destabilizing surface buoyancy flux $J_b(0)$ and wind stress $\boldsymbol{\tau}_w$. The nocturnal mixing-layer depth z_{ML} can be inferred by comparing the available potential energy APE in the stratification $N^2(z)$ in the water column prior to destabilizing forcing with the time integral of the power being input by surface forcing

$$\Delta\mathrm{APE} = \int_{z_{\mathrm{ML}}}^{0} N^2(z) z\, dz = \int_0^t \left[J_b(0) - \frac{\gamma(\mathbf{v}_0 \cdot \boldsymbol{\tau}_w)}{\rho_0 z_{\mathrm{ML}}} \right] dt, \qquad (2)$$

where mixing efficiency $\gamma \sim 0.2$ is assumed for wind-driven turbulent mixing (Gregg et al. 2018) while unity efficiency for destabilizing buoyancy fluxes (Shay and Gregg 1986). This bulk formula neglects destratification or restratification by lateral processes such as geostrophic adjustment, mixed-layer eddies and Ekman buoyancy flux since vertical 1D processes dominate during the nights of 24–27 March.

Nocturnal mixing-layer depth z_{ML} inferred from surface buoyancy fluxes alone, or surface buoyancy fluxes plus wind stress (2), are compared with observed mixing-layer deepening in Fig. 7. For 24 March, (2) was applied incrementally every hour while, starting on 25 March, the pre-nighttime N^2 profile

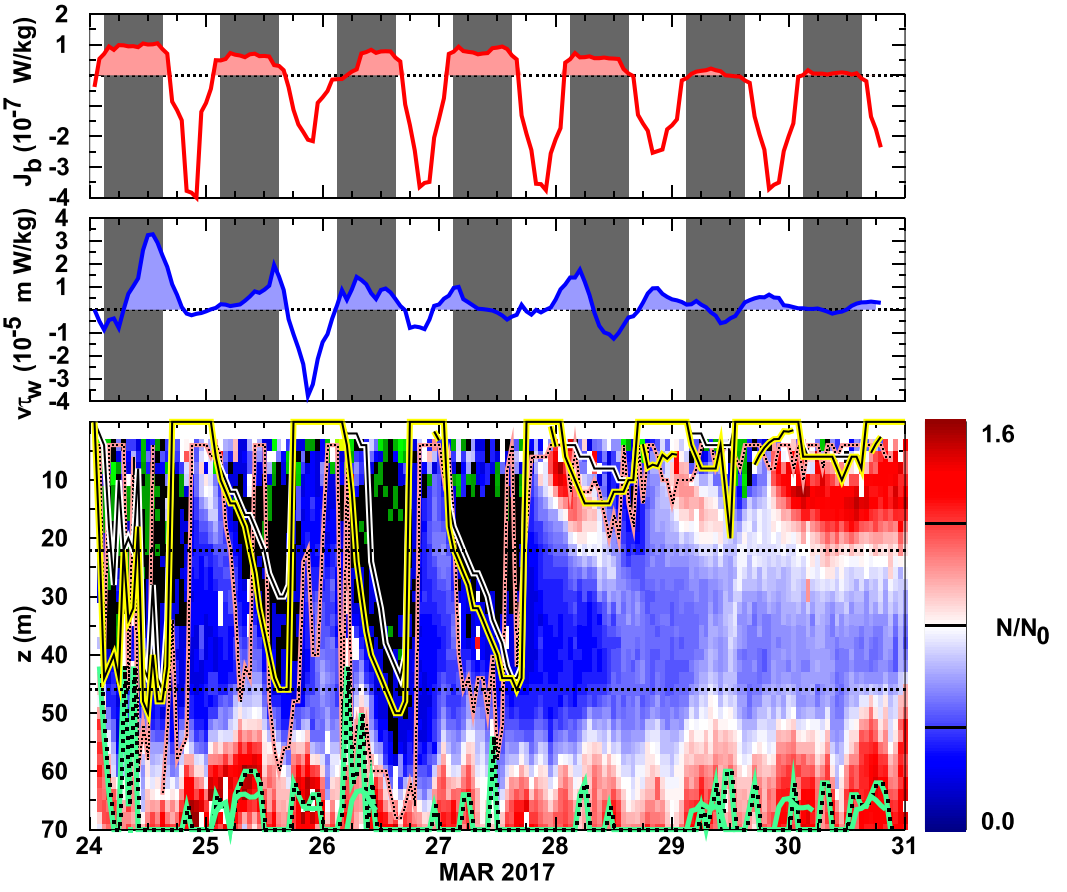

FIG. 7. As in Fig. 3, but with (top) surface buoyancy flux $J_b(0)$ and (middle) wind-work $\mathbf{v} \cdot \boldsymbol{\tau}_w/\rho_0$ (shaded destabilizing). Gray bars denote local night. (bottom) Normalized buoyancy frequency N/N_0, where $N_0 = 5 \times 10^{-3}$ rad s^{-1}, black denotes $N^2 = 0$, and green $N^2 < 0$. Solid black lines denote predictions for penetration of destabilizing surface forcings (2). The white–black–white line takes into account only destabilizing surface buoyancy fluxes $J_b(0)$ while the yellow–black–yellow line includes wind-work $\gamma\mathbf{v} \cdot \boldsymbol{\tau}_w$, where $\mathbf{v}$ is the float array average in the upper 10 m. The mixed-layer thickness based on a density difference > 0.03 relative to the 2-m depth value (pink highlighted dotted) resembles curves based on surface forcing but not perfectly. The pale green highlighted black dotted curve near the lower axis is the depth of the highest stratification in the underlying pycnocline.

was used for the time integration, measured $N^2(z)$ being bin averaged over 1 h, 2 m and the float array in both cases. Wind power was initially strong due to the 23 March storm, then weakened over the course of the sampling, as do destabilizing nocturnal buoyancy fluxes, such that, by the end of the time series, daytime warming dominated surface forcing. The bulk of mixing-layer deepening prior to 28 March is due to surface buoyancy-flux forcing, but the addition of wind-stress forcing improves comparison with measured N^2 profiles (Fig. 7). The nocturnal mixing layer extends almost to the base of the weakly stratified surface boundary layer on 25 and 26 March. The presence of both weakly stable (blue) and unstable (green) stratification in the upper nocturnal mixing layer is interpreted as a signature of active convection. After 28 March, destabilizing buoyancy fluxes and wind stresses are weak, so that nocturnal mixing-layer deepening is confined above ~20-m depth. While weak, inclusion of wind stress is necessary to reproduce deepening of the mixing layer and capping of the stratified TL. The slowness of mixing-layer shoaling on the mornings of 28 and 29 March (Fig. 7) is also attributed to wind-forcing acting against stabilizing daytime buoyancy fluxes. Defining the mixed-layer depth by a 0.03 kg m^{-3} density difference with the shallowest measurement (de Boyer Montégut et al. 2004) is broadly consistent with tendencies from the bulk energy approach (2) but tends to be sensitive to small fluctuations in density profiles as previously noted (e.g., Haine and Marshall 1998; Sutherland et al. 2014).

5. Restratification and the stratification budget

Shoaling and weakening of nocturnal destratification (Figs. 3 and 7) sets the stage for restratification of the surface layer

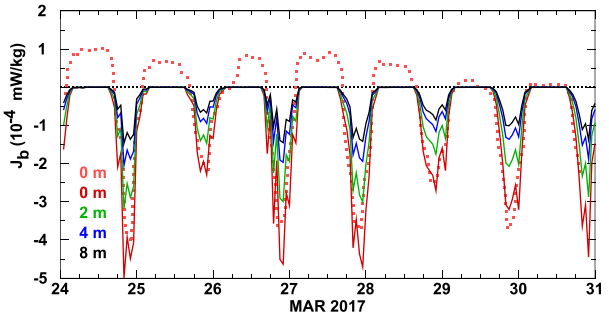

FIG. 8. Air–sea buoyancy fluxes at the surface $J_b(0)$ (red dotted) and shortwave penetrative radiation buoyancy fluxes $J_b(z)$ in the upper surface layer following Paulson and Simpson (1977) (solid). Destabilizing nocturnal buoyancy fluxes weaken on 29 and 30 Mar due to weakening winds and latent heat-fluxes. Restratifying daytime buoyancy fluxes are weaker on 25, 28, and 29 Mar.

by shortwave penetrative radiation buoyancy fluxes $J_b(z)$, diapycnal turbulent buoyancy fluxes $\langle w'b'\rangle$ and vertical shearing of horizontal buoyancy gradients $u_z b_x + v_z b_y$. In this section, measured restratification in the daytime surface layer before 28 March and ~22–46-m remnant layer after 28 March will be compared to contributions from penetrative radiation, turbulent buoyancy flux, and horizontal advection in a stratification budget framework. Vertical heaving and straining, as well as residual horizontal displacements that arise because the float array is not perfectly Lagrangian with respect to the surface layer, are confirmed to be small.

Starting from buoyancy conservation

$$\frac{Db}{Dt} = \frac{\partial b}{\partial t} + ub_x + vb_y + wb_z = -\frac{\partial \langle w'b'\rangle}{\partial z} - \frac{\partial J_b(z)}{\partial z}, \qquad (3)$$

where buoyancy $b = -g\rho'/\rho_0$, density anomaly $\rho'(x, y, z, t) = \rho(x, y, z, t) - \rho_0$ includes density perturbations due to thermal wind and internal waves as well as surfaced-forced restratification, gravitational acceleration $g = 9.78\,\mathrm{m\,s^{-2}}$, $\rho_0 = 1028.1\,\mathrm{kg\,m^{-3}}$, turbulent buoyancy flux is $\langle w'b'\rangle$, and shortwave penetrative radiation buoyancy flux is $J_b(z)$. Evolution of stratification $N^2 = b_z$ in the surface layer can be treated in a horizontally Lagrangian framework following the EM float array by taking the vertical derivative of (3)

$$\frac{D_h N^2}{D_h t} = \frac{D_h b_z}{D_h t} = -u_z b_x - v_z b_y - w_z b_z - wb_{zz} + \frac{\partial^2}{\partial z^2}\left[\frac{N^2\chi_T}{2\langle T_z\rangle^2}\right] - \frac{\partial^2 J_b(z)}{\partial z^2}, \qquad (4)$$

where $D_h/D_h t$ is the time rate of change in a Lagrangian frame. It is assumed that (i) residual horizontal advection $uN_x^2 + vN_y^2 = ub_{xz} + vb_{yz}$ can be neglected following the semi-Lagrangian drifting float array as in Johnson et al. (2020a), consistent with lateral displacements of the surface layer relative to the array being a factor-of-2 smaller than the array dimensions (section 2). The lack of depth dependence in the measured surface-layer horizontal buoyancy gradients, that is, $b_{xz} \sim b_{yz} \sim 0$ (Figs. 5a,c), also supports neglect of these terms.

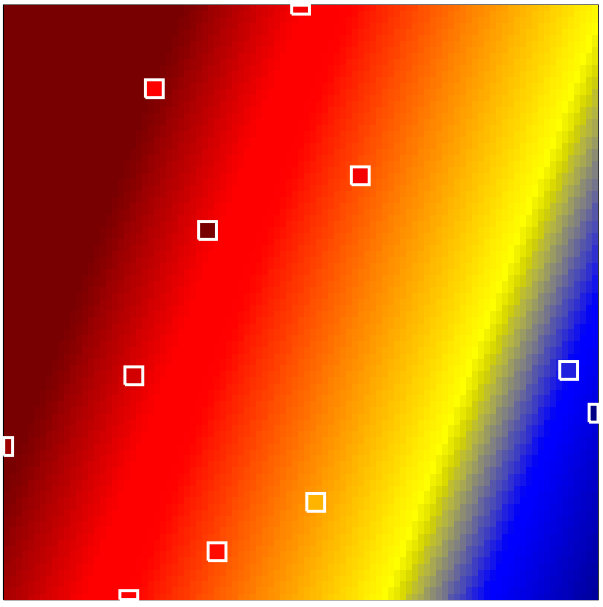

FIG. 9. One of ~5000 least squares plane fits to buoyancy b in 1-h and 2-m bins over the ~5-km EM float array to obtain horizontal buoyancy gradients (b_x, b_y). The horizontal and vertical axes are the longitude and latitude range of the array for the time-depth bin. The box is roughly 2′ on a side. Filled color is the plane fit $b_0 + b_x x + b_y y$ ranging from minimum to maximum float buoyancies while float locations and buoyancies are boxed in white. This example is from 40-m depth during mid 24 Mar.

It is also assumed that (ii) the diapycnal diffusivity for buoyancy $K_b = -\langle w'b'\rangle/N^2$ (Osborn 1980) is the same as the turbulent thermal diffusivity $K_T = \chi_T/(2\langle T_z\rangle^2)$ (Osborn and Cox 1972) without need to invoke a mixing coefficient γ because measured χ_T is a more direct measure of turbulent buoyancy flux, $\langle w'b'\rangle = -N^2\chi_T/(2\langle T_z\rangle^2)$, than dissipation rate ε in stably stratified conditions. However, turbulent buoyancy fluxes $\langle w'b'\rangle$ cannot reliably be estimated from our χ_T measurements using local gradients and diffusivities (Osborn and Cox 1972) in waters influenced by surface-forced convection, where bulk parameterizations of ''nonlocal'' mixing are typically employed (e.g., (2), Price et al. 1986, and in the KPP model of Large et al. 1994), preventing quantification in the ML and TL. This limits measured turbulent buoyancy-flux estimates (4) to the daytime stratifying surface layer prior to 28 March and stratified remnant layer starting on 28 March.

Following the EM float array, we can estimate evolution of surface-layer stratification N^2 and contributions to restratification from penetrative radiation, turbulence, and horizontal advection in (4) at site 3 (35°6.16′N, 139°33.51′W) during 24–31 March 2017:

- Penetrative radiation buoyancy fluxes $J_b(z)$ are inferred from shipboard air–sea flux measurements and the Paulson and Simpson (1977) parameterization (section 2, Fig. 8) to be $J_b = 10^{-9}$–$10^{-7}\,\mathrm{W\,kg^{-1}}$ during daylight with the expected surface-intensified signal (Fig. 10h). Uncertainties in penetrative radiation contributions are less than 6%.

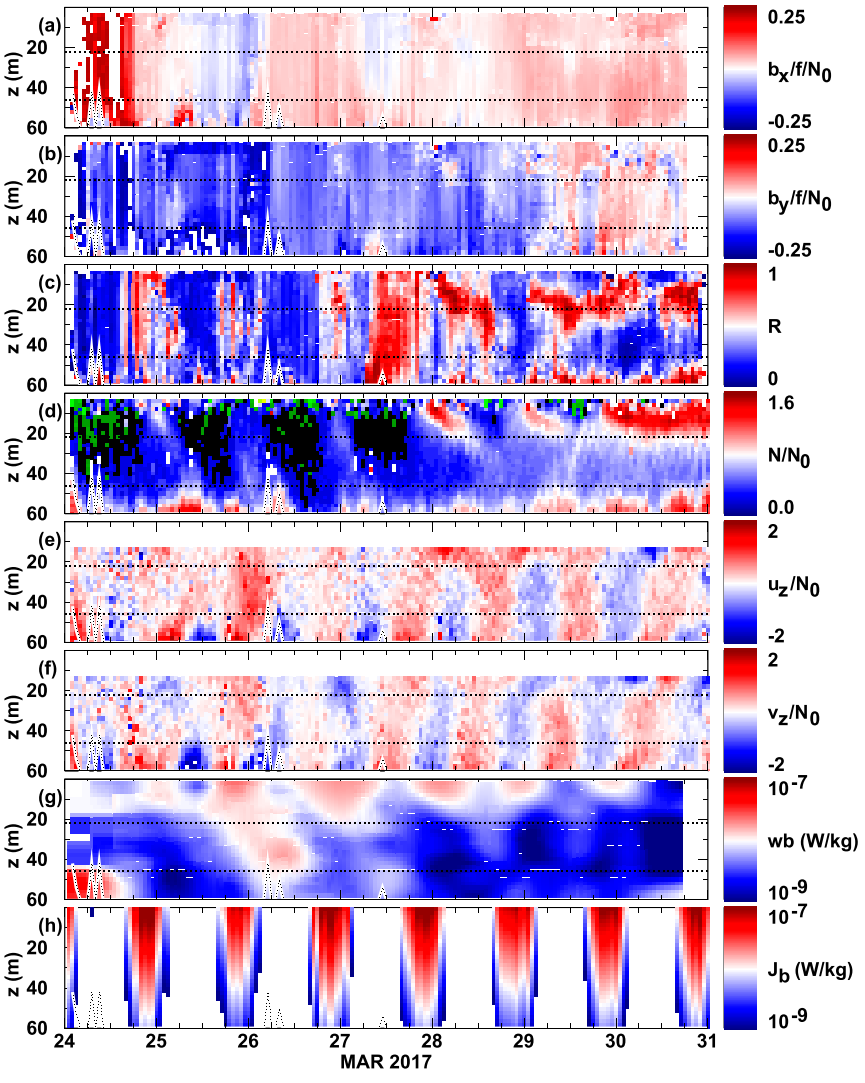

FIG. 10. Profile time series of normalized (a) zonal buoyancy gradient $b_x/f/N_0$, (b) meridional buoyancy gradient $b_y/f/N_0$, (c) residual buoyancy variance ratio R, (d) buoyancy frequency N/N_0 (black denotes $N^2 = 0$, green $N^2 < 0$), (e) zonal vertical shear u_z/N_0, (f) meridional vertical shear v_z/N_0, (g) turbulent buoyancy-flux magnitude $|\langle w'b'\rangle| = \chi_T N^2/(2T_z^2)$, and (h) shortwave penetrative radiation buoyancy flux J_b, all bin-averaged over 1 h, 2 m, and the EM float array. Normalizing buoyancy frequency $N_0 = 5 \times 10^{-3}$ rad s^{-1} and Coriolis frequency $f = 0.8 \times 10^{-4}$ rad s^{-1}. Inertial/diurnal oscillations dominate vertical shears in (e) and (f), exhibiting slight upward phase propagation (downward energy propagation). Both inferred turbulent diapycnal buoyancy-flux magnitudes $|\langle w'b'\rangle|$ in (g) and penetrative radiation buoyancy fluxes J_b in (h) range over 10^{-9}–10^{-7} W kg^{-1}.

- Vertical buoyancy gradients $N^2 = b_z$ (Fig. 10d) and vertical shears u_z and v_z are array-binned over 1 h and 4 m every 2 m. Thus, semidiurnal, inertial/diurnal, and subinertial contributions are included. Vertical shears are predominantly inertial/diurnal with weak upward phase propagation (Figs. 10e,f), that is, clockwise rotary in time and depth, as previously reported (Hosegood et al. 2008). Vertical shears are noisy and unreliable above ~15-m depth, likely because of surface-wave contamination (Sanford et al. 2011; Hsu et al. 2018).
- Horizontal buoyancy gradients b_x and b_y are based on linear least squares plane fits over the ~5-km EM float array in the same 1-h and 2-m bins after discarding 10% of the outliers in each bin (Fig. 9). These can be unreliable if the array is strained into a 1D line, but this is not an issue at site 3. The quality of individual fits was measured as the ratio R of the residual over raw buoyancy variance (Fig. 10c) with $R = 0$ representing a perfect fit and fits discarded if $R > 0.5$, though excluding or including fits with large residuals proved not to impact the time-integrated shearing advective restratification

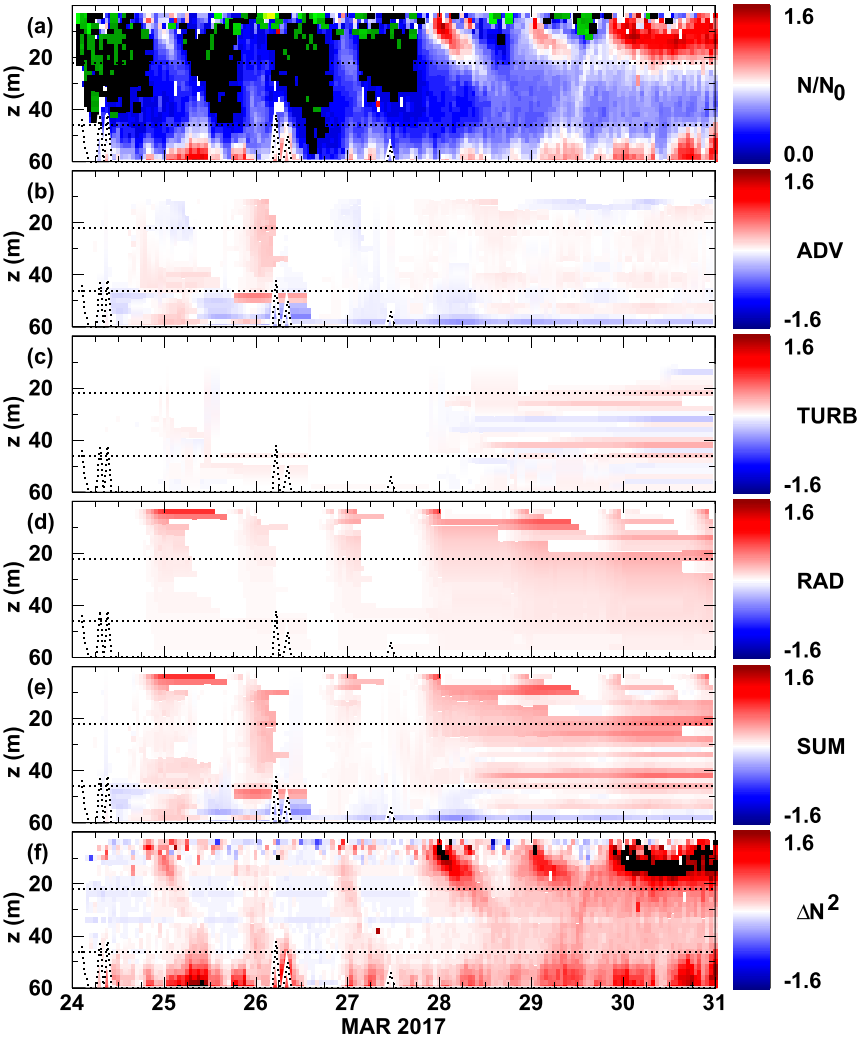

FIG. 11. Profile time series of normalized (a) buoyancy frequency N/N_0 (black indicates $N^2 = 0$, green $N^2 < 0$), along with time integrals from (6)–(8) of (b) vertical shearing of horizontal buoyancy gradients $\int(u_z b_x + v_z b_y)\,dt$ (ADV), (c) turbulent diapycnal buoyancy-flux curvature $\int\langle w'b'\rangle_{zz}\,dt$ (TURB), (d) penetrative radiation buoyancy-flux curvature $\int J_{bzz}\,dt$ (RAD), (e) sum of advective, turbulent, and radiative contributions $\sum \delta N^2$, and (f) measured stratification anomaly ΔN^2 relative to a profile with a deep well-mixed layer near the beginning of the record. Panels (b)–(f) are normalized by $N_0^2 = 2.5 \times 10^{-5}\,\mathrm{s}^{-2}$. The surface layer exhibits diurnal destratification and restratification during 24–27 Mar, then restratifies in a TL above 20 m and an RL between 22 and 46 m until 31 Mar. Penetrative radiation in (d), turbulence in (c), and advection in (b) all contribute to net restratification in (e) in the remnant layer, but advection is small except on 26 Mar and turbulence small before 28 Mar.

$\int(u_z b_x + v_z b_y)\,dt$. Horizontal buoyancy gradients (b_x, b_y) are dominated by depth-independent subinertial variability (Figs. 10a,b). This coherence in depth and time lends confidence to the reliability of these estimates.

- Turbulent buoyancy fluxes are also averaged in 1-h and 2-m bins over the float array. Turbulent buoyancy fluxes $\langle w'b'\rangle = -\langle N^2\chi_T/(2T_z^2)\rangle \sim 10^{-9}$–$10^{-7}\,\mathrm{W\,kg^{-1}}$ are influenced by diurnal surface forcing. They are weak in the RL below 20-m depth starting on 26 March (Fig. 10g). As already described, these are not reliable when mixing is surface-forced, that is, in mixing and transition layers. The lognormal nature of turbulence makes this contribution to restratification uncertain in general; a single large event can have lasting impact. The second derivative with depth enhances random noise.

Measured restratification, through the evolving stratification anomaly

$$\Delta N^2(z, t) = N^2(z, t) - N_i^2(z, t_0) \tag{5}$$

(Fig. 11f), where $N_i^2(z)$ is a typical late-night profile of very weak surface-layer stratification [$N_i^2(z) \sim 0$] from early 24 March (Fig. 11a), is compared to time-integrated contributions from (4) of (i) penetrative radiation buoyancy flux J_b curvature

$$\delta N_r^2 = -\int \frac{\partial^2 J_b}{\partial z^2}\, dt \tag{6}$$

(Fig. 11d), (ii) inferred diapycnal turbulent buoyancy flux $\langle w'b' \rangle$ curvature

$$\delta N_t^2 = -\int \frac{\partial^2 \langle w'b' \rangle}{\partial z^2}\, dt = \int \frac{\partial^2}{\partial z^2}\left[\frac{\chi_T N^2}{2\langle T_z \rangle^2}\right] dt \tag{7}$$

(Fig. 11c), and (iii) vertical shearing of horizontal buoyancy gradients

$$\delta N_a^2 = -\int (u_z b_x + v_z b_y)\, dt \tag{8}$$

(Fig. 11b), where the time integrals $\int dt$ reduce random noise in the estimates below 10% after 25 March. The vertical shearing horizontal advection term $u_z b_x + v_z b_y$ leads to an increase in the vertical buoyancy gradients b_z by steepening isopycnal slopes. This term can also reduce b_z by tilting buoyancy gradients into the horizontal, limited by overturning when $N^2 < 0$. Because only vertical shears contribute to buoyancy advective restratification (8), there is no need to make the velocity profiles absolute and velocity uncertainties are smaller, ~0.5 cm s^{-1} (section 2).

The measured stratification anomaly ΔN^2 (5) and integrals (6)–(8) are reset to zero whenever local $N^2 \leq 0$ (Fig. 11a). Measurements and assumptions are unreliable above ~20-m depth because of inadequate vertical resolution, surface-wave contamination of vertical shear and surface-forced convective buoyancy fluxes which cannot be inferred reliably from Osborn and Cox (1972). They are also unreliable near the base of the surface layer ($z > 50$ m) because of heaving of the pycnocline. At intermediate surface-layer depths (associated with the remnant layer after 28 March), uncertainties in measured ΔN^2 (5) are less than 5% and those in the sum of the individual contributions $\sum \delta N^2$ (6)–(8) less than 15%.

Penetrative radiation curvature $\partial^2 J_b/\partial z^2$ (6) dominates over turbulence curvature (7) and advection (8) in the upper ~20 m (Fig. 11) except on 26 March when advective restratification exhibits a large daytime signal throughout the surface layer. However, the sum of contributions $\sum \delta N^2$ at these depths (Fig. 11e) falls short of the measured ΔN^2 (Fig. 11f) because formation of a strongly stratified transition layer on 28 March is due to nonlocal surface-forced convective buoyancy fluxes.

Time series of measured stratification anomaly ΔN^2 (5) along with integrated contributions δN^2 from penetrative radiation (RAD) (6), turbulent buoyancy flux (TURB) (7), and horizontal advection (ADV) (8) at five depths spanning 22–44-m depth in the center of the surface layer (remnant layer starting on 28 March) emphasize the different character before and after 28 March (Fig. 12). Prior to 28 March, the measured anomaly ΔN^2 exhibits peaks late in the day that are qualitatively reproduced by penetrative radiation and advection, with turbulence making little contribution. Starting on 28 March, ΔN^2 no longer goes to zero at night but increases in the RL with penetrative radiation stepping up stratification every day, turbulence making less regular but mostly positive contributions, and advection weak and more oscillatory. Overall, penetrative radiation and turbulence contribute the bulk of restratification while advection has little impact except on 26 March. The sum of contributions $\Sigma\, \delta N^2$ appears comparable to ΔN^2 except for strong transient shortfalls (red stars in Fig. 12), particularly on the nights of 28 and 29 March. These transient discrepancies will be discussed at the end of this section where it is shown that model shortfalls are due to breakdowns in the assumptions of no influence on the remnant layer by (i) nonlocal convection from above and (ii) heaving of the underlying pycnocline from below.

Corrections for vertical heaving

$$\int w b_{zz}\, dt = \frac{\partial N^2}{\partial z}(z + \xi),$$

and straining

$$\int w_z b_z\, dt = \xi_z N^2$$

(4) are based on rms heaving of ~5 m by the $\sigma_\theta = 25.22$ isopycnal near the top of the pycnocline (65–70-m depth, Fig. 3) and assuming $\xi = w = 0$ at the surface ($z = 0$). Because of their mostly short-time-scale reversible contribution, vertical heaving and straining represent less than an rms 10% perturbation to surface-layer thickness and stratification, smaller than uncertainties and transient discrepancies between ΔN^2 (5) and $\sum \delta N^2$ (6)–(8). Better resolving w within the surface layer by tracking isopycnal displacements is not possible because surface-layer density is not conserved.

The sum of contributions $\sum \delta N^2$ (6–8) resembles measured ΔN^2 (8) though there are transient underestimates of large ΔN^2 peaks at 22–34 m during local nighttime on 28 March and 22, 34–44 m on 29 March (red stars in Fig. 12). With advective restratification $\int (u_z b_x + v_z b_y)\, dt$ accounted for, and vertical heaving and strain corrections small, the shortfall must have another cause. Examination of the discrepancy intervals reveals that the ΔN^2 peaks are due to a small fraction of float profiles (<20% at 22 m, and <10% at greater depths) with much elevated N^2 (Fig. 13). For the ΔN^2 peaks above 35 m, the overlying water column in these anomalous profiles was well-mixed relative to the bulk of the profiles but with the same depth-average density (Fig. 13a), suggesting that localized convective mixing has homogenized the overlying water column and sharpened stratification at the base of the mixing layer. These occurrences were in isolated profiles with lateral coherence < 0.5 km and temporal coherence < 1 h. For the ΔN^2 peaks below 35 m, elevated stratification appears to be due to uplift of the underlying permanent pycnocline above the $\sigma_\theta = 25.22$ surface (Fig. 13b), again in only a few float profiles. These deeper anomalous profiles

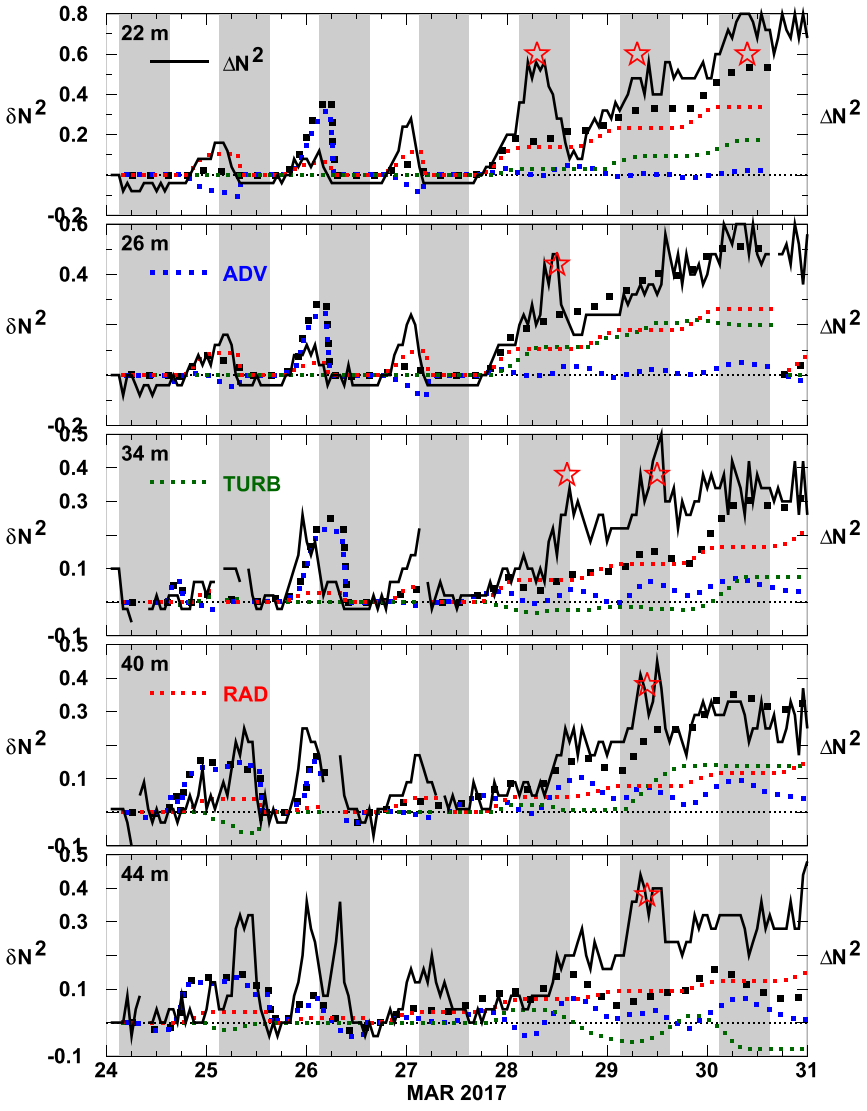

FIG. 12. Comparison of normalized measured restratification $\Delta N^2/N_0^2$ (black solid) with contributions from the time integrals of shortwave penetrative radiation curvature (red dot), turbulent buoyancy-flux curvature (green dot), horizontal advection (blue dot), and the sum of these three contributions $\sum \delta N^2/N_0^2$ (black dot) at remnant-layer depths of 22–44 m. ΔN^2 and δN^2 are normalized by $N_0^2 = 2.5 \times 10^{-5}\,\mathrm{s}^{-2}$. Penetrative radiation, horizontal advection, and turbulence all contribute. Their sum $\sum \delta N^2$ reproduces the measured restratification ΔN^2 within ~15% uncertainties, particularly and 26 and 40 m, except during transient nocturnal ΔN^2 peaks (red stars) at all depths on 28–30 Mar. Starting on 28 Mar, penetrative radiation and turbulence dominate while advection is weak and sometimes destratifying.

showed more coherent lateral structure that persisted for more than a day. Thus, the discrepancies between ΔN^2 and $\sum \delta N^2$ are due to exceptions to our assumptions arising in a small fraction of the float profiles. These spatially and temporally localized anomalies, where either the transition layer or pycnocline intrudes into the remnant layer, are transient (Fig. 12) so that, overall, model (4) reproduces observed remnant-layer restratification at depths of 22–40 m.

In summary, prior to 28 March, the primary restratification mechanisms are advection and penetrative radiation with turbulent buoyancy fluxes making little contribution (Fig. 12). Starting on 28 March in the remnant layer, penetrative radiation and turbulence predominate with advection playing little role. Episodic shortfalls of $\sum \delta N^2$ (6)–(8) relative to measured ΔN^2 (5) (red stars in Fig. 12) arise from transient incoherent intrusions from above or below the remnant layer belying the assumption of its isolation (Fig. 13) but having no long-term impact.

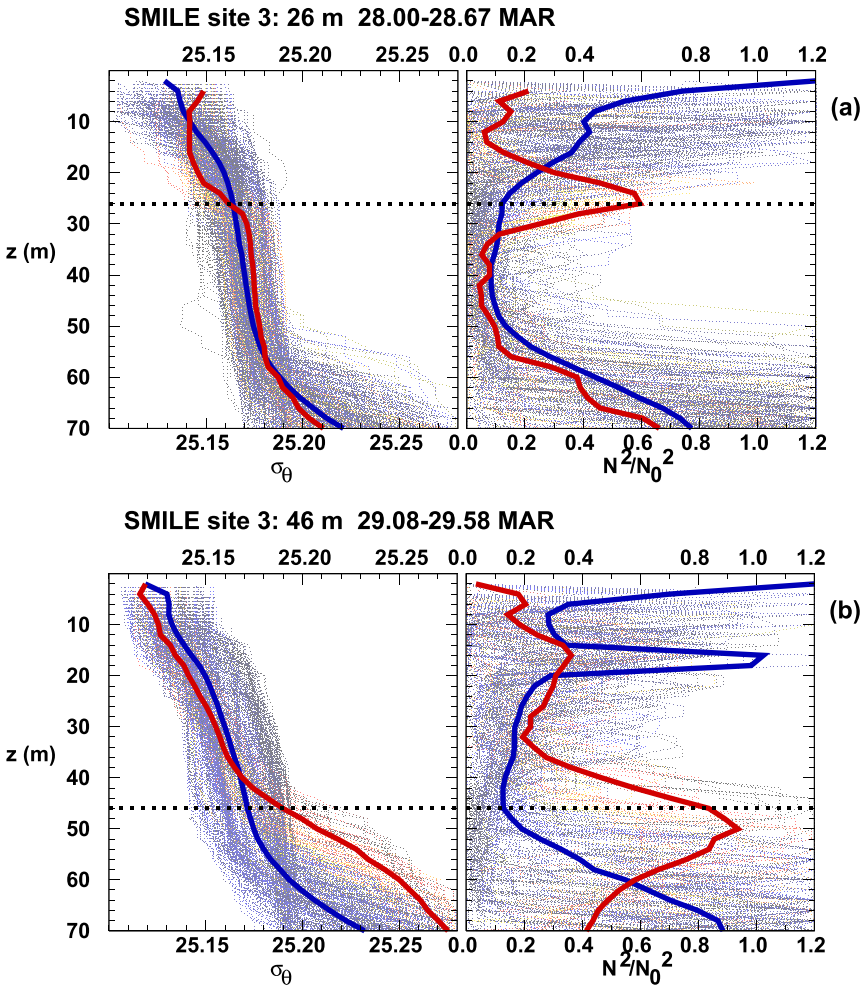

FIG. 13. (left) Average density σ_θ and (right) normalized stratification N^2/N_0^2 profiles for the ΔN^2 peak periods at (a) 26 m on 28 Mar representing 22–34-m ΔN^2 peaks in Fig. 12 (red stars) and (b) 46 m on 29 Mar representing 40–46-m ΔN^2 peaks. Dotted horizontal lines mark the target ΔN^2 peak depths. Most (>80%) float profiles during these depth–time intervals do not have high N^2 (blue curves). A small fraction (red curves) is responsible for the ΔN^2 peaks in Fig. 12. For the $z < 35$ m ΔN^2 peaks (a), the overlying water column is well-mixed in the high-ΔN^2 profiles (left) such that stratification is sharpened at the base of this homogenized layer (right). For the $z > 35$ m ΔN^2 peaks in (b), elevated stratification (right) at the designated depth (dotted line) is associated with uplift of the permanent pycnocline (left). Thus, remnant-layer ΔN^2 peaks in Fig. 12 are due to two independent mechanisms involving intrusion either from above or below.

6. Advective contribution

Irrespective of whether shortwave penetrative radiation dominates restratification ΔN^2, the measured advective contribution (8) can be compared with (i) geostrophic adjustment

$$\frac{b_h^2}{f^2}[1-\cos(ft)] \tag{9}$$

(Tandon and Garrett 1994), which arises from relaxation of an unbalanced horizontal buoyancy gradient into a thermal-wind balance plus inertial oscillations, fluctuating between b_h^2/f^2 and zero, (ii) the MLE parameterization

$$(u_z, v_z)\cdot(b_x, b_y) = \psi_{zz}|\nabla_h b| = C_e H^2 \mu_{zz}\int\frac{b_h^2}{|f|}dt, \tag{10}$$

where $C_e = 0.06$,

$$H^2\mu_{zz} = \frac{16}{21}(8+15x^2) \tag{11}$$

(Fox-Kemper et al. 2008; Johnson et al. 2020a) and $x = 1 + 2z/H$, with maxima of $16 \times 23/21 \sim 17.5$ at the top and bottom of the surface layer independent of surface-layer thickness H, and (iii) Ekman buoyancy flux

$$\mathrm{EBF} = \frac{(\boldsymbol{\tau}_w \times \hat{\mathbf{k}}) \cdot \nabla_h b}{\rho_0 f} = \frac{(\tau_x b_y - \tau_y b_x)}{\rho_0 f} \tag{12}$$

(Thomas and Lee 2005; Taylor and Ferrari 2010) with the contribution of EBF to restratification and destratification

$$\int \frac{\mathrm{EBF}}{H^2}\, dt, \tag{13}$$

assumed to be uniformly distributed over the $H = 55$-m thick surface layer. During the latter half of the time series, it is more likely that Ekman fluxes will be confined to the mixing and transition layers above ~20-m depth so will not contribute to remnant-layer restratification, that is, bulk parameterization (13) is not appropriate in the RL, but it is instructive to see what impact it might have. Neither Ekman buoyancy flux nor transient turbulent thermal wind (Dauhajre and McWilliams 2018; Johnson et al. 2020b) can be evaluated with any fidelity because turbulent momentum fluxes were not measured. Geostrophic adjustment and MLE instability are necessarily positive definite because they extract frontal APE by relaxing horizontal buoyancy gradients into the vertical. Subinertial MLE instabilities arise after a front has slumped and adjusted geostrophically (Boccaletti et al. 2007; Fox-Kemper and Ferrari 2008; Fox-Kemper et al. 2008). Their ageostrophic circulation has stronger vertical than horizontal buoyancy fluxes. However, these vertical fluxes are adiabatic so can only redistribute stratification within the surface layer, sharpening it at the top and base while weakening it in the middle without changing the bulk surface-layer stratification $(1/H)\int N^2(z)\, dz$.

The measured advective restratification (8) fluctuates on inertial/diurnal time scales (Fig. 14a), more strongly in the beginning of the time series, because of both inertial shear throughout the record and nocturnal destratification prior to 28 March (Fig. 10). It exhibits strong destabilizing tendencies at the base of the surface layer (~45–60 m) during 24–26 March (Fig. 14a), while the MLE parameterization (10) is strongly restratifying by construction, but is otherwise almost depth-independent, and only weakly and semiperiodically destabilizing. Its magnitude (Fig. 14b) is stronger than the MLE parameterization (Fig. 14d) above ~40-m depth. This is likely because measured vertical shear scales as $\sim N$ and measured horizontal buoyancy gradients as $\sim 0.1fN$ so that $v_z b_h$ scales as $\sim 0.1fN_0^2$ while the MLE parameterization b_h^2/f scales as $0.01fN_0^2$. It is reset to zero by $N^2 \le 0$ like the measured buoyancy advective restratification (Figs. 14a,b). Shallower than ~45-m depth, this occurs every night before 28 March (Fig. 7). Below 45-m depth, destratification reset occurs only once, in the middle of 26 March, after the strongest MLE restratification. This destratification event is due, not to surface forcing, but near-inertial shear-driven convection via $u_z b_x + v_z b_y$. After 28 March, the measured buoyancy advective restratification and MLE parameterization have more comparable magnitudes. The contribution from inertially smoothed vertical shear and horizontal buoyancy gradients (Fig. 14c) retains restratifying and destratifying oscillations above 40-m depth because of nocturnal resets before 28 March but closely resembles MLE (Fig. 14d) below 40 m after 28 March.

Comparison of measured advective restratification $\int (u_z b_x + v_z b_y)\, dt$ with all three parameterizations at remnant-layer depths 22–44 m (Fig. 15) further emphasizes the oscillatory inertial nature of measured advective restratification. Prior to 28 March, measured advective restratification both restratifies and destratifies during the day, particularly on 26 and 27 March, due to storm-driven inertial shear. It is much stronger than any of the parameterizations though geostrophic adjustment and MLE exhibit similar behavior at ~44-m depth. After 28 March, measured $\int (u_z b_x + v_z b_y)\, dt$ tends to be restratifying and its subinertial envelope resembles the MLE parameterization (10) while geostrophic adjustment (9) is limited to oscillating between zero and b_h^2/f^2. The resemblance of MLE to $\int (u_z b_x + v_z b_y)\, dt$ suggests that we have captured MLE instability during its early stages of growth, even while shortwave penetrative radiation and turbulent buoyancy fluxes dominate restratification of the surface layer.

Unlike geostrophic adjustment and MLE, Ekman buoyancy flux can be either restratifying or destratifying. But, prior to 28 March, it is uncorrelated with the measurements. After 28 March, bulk EBF (13) resembles the subinertial envelope of the measured advective restratification and the MLE parameterization. However, as already discussed, Ekman fluxes are unlikely to extend into the remnant layer.

In summary, measured daytime advective contribution in the first half of the record is dominated by both restratification and destratification driven by storm-forced inertial shear while the subinertial envelope of measured advective restratification resembles MLE parameterization (10) in the isolated remnant layer starting on 28 March. This lends support to MLE instability theory in the absence of destabilizing surface forcing.

7. Summary

The evolution of spring surface boundary layer (SL) stratification in the North Pacific Subtropical Front at 35°N, 140°W in the wake of a storm (Fig. 1) was examined with a ~5-km array of 23 synchronously profiling EM-APEX floats (u, v, T, S, P) augmented with FP07 microstructure temperature sensors (χ_T) (Fig. 2). The role of 3D shear advection $u_z b_x + v_z b_y$ in surface-layer restratification was quantified from simultaneous and collocated 1-h- and 2-m-binned vertical shear (u_z, v_z) (Figs. 10e–f) and lateral buoyancy gradients (b_x, b_y) (Figs. 10a,b) based on ~5-km least squares plane fits (Fig. 9). While 1D shortwave penetrative radiation (Fig. 10h) and turbulent buoyancy fluxes (Fig. 10g) dominated restratification processes, subinertial advective restratification was consistent with the MLE parameterization in the remnant layer after nocturnal destratification weakened.

We identify three regimes in the SL (Fig. 3): (i) an actively convective mixing layer (ML) set by destabilizing surface buoyancy- and wind-forcing (2), (ii) a stratified transition layer (TL) below the mixing layer starting on 28 March that is also influenced by nonlocal surface-forced convection, and (iii) a remnant layer (RL) below the transition layer starting on 28 March that is isolated from destabilizing surface forcing. Only local turbulent buoyancy fluxes (7) could be inferred using the EM float χ_T measurements with the

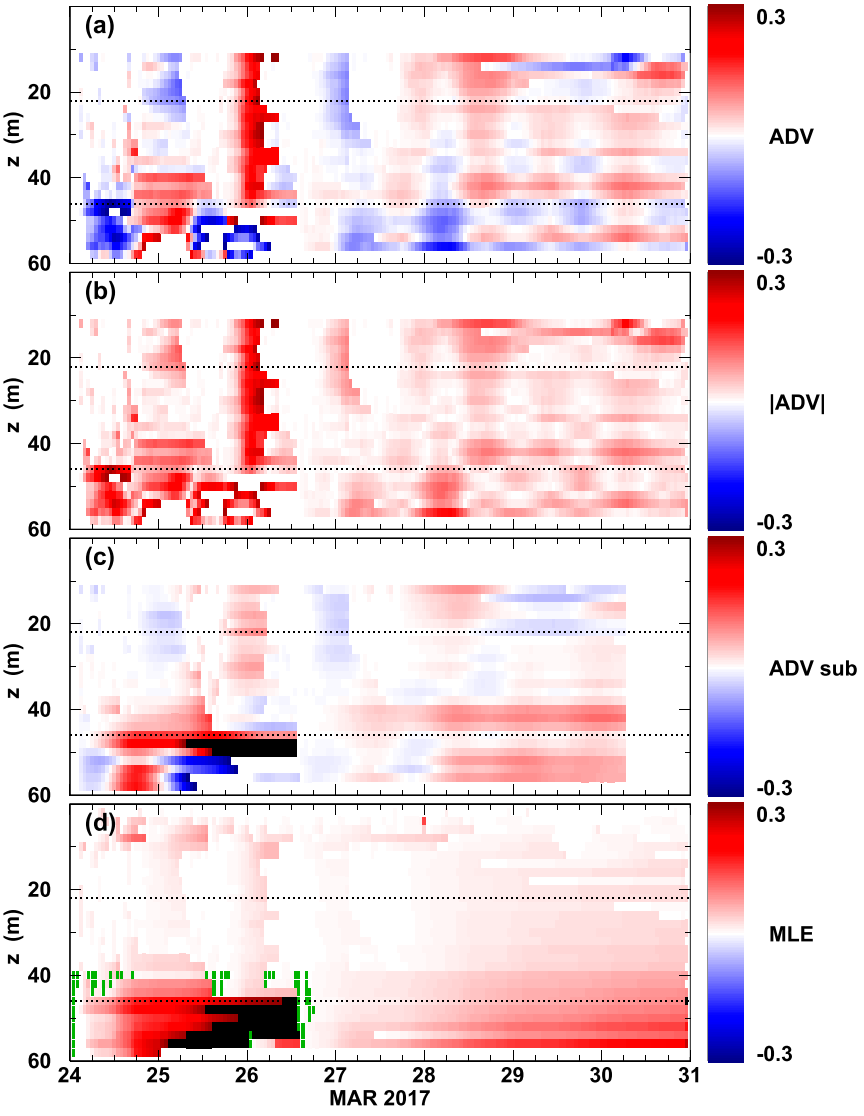

FIG. 14. Profile time series comparing (a) normalized measured advective restratification $\int(u_z b_x + v_z b_y)\,dt/N_0^2$ ($N_0 = 5 \times 10^{-3}\,\mathrm{rad\,s^{-1}}$) (4, 8), (b) its absolute value, and (c) subinertial contribution with (d) Boccaletti et al. (2007) MLE instability parameterization $C_e \mu_{zz} \int B_h^2\,dt/f/N_0^2$ (10). Green in (d) marks $N^2 < 0$ below 40-m depth. Measured restratification in (a) both restratifies and destratifies while MLE in (d) is positive definite. Measured advective restratification is approximately depth-independent and exhibits inertial/diurnal fluctuations, even in the 22–46-m-depth RL starting on 28 Mar, while MLE is intensified toward the base of the surface layer and is subinertial. Measured subinertial advective restratification based on inertially smoothed vertical shears and horizontal buoyancy gradients in (c) is still affected by nocturnal resets before 28 Mar and exhibits destratifying events through the record above 40-m depth. It resembles MLE predictions below 40 m in (d). Strong oscillating restratification and destratification below 40-m depth before 27 Mar in (a) are due to both strong horizontal buoyancy gradients and strong storm-forced inertial shears, terminating mid–26 Mar when $N^2 \leq 0$ due to near-inertial shear-driven convection.

Osborn and Cox (1972) mixing relation, which limits reliable estimates to stratified regions not influenced by nonlocal surface-forced convection. Therefore, stratification budgets (4) are confined to the daytime stratifying surface layer before 28 March, and RL depths of ~22–46 m below the mixing and transition layers, and above the heaving base of the SL, starting on 28 March.

During the first four days (prior to 28 March), nocturnal destabilizing buoyancy fluxes mixed the surface layer over

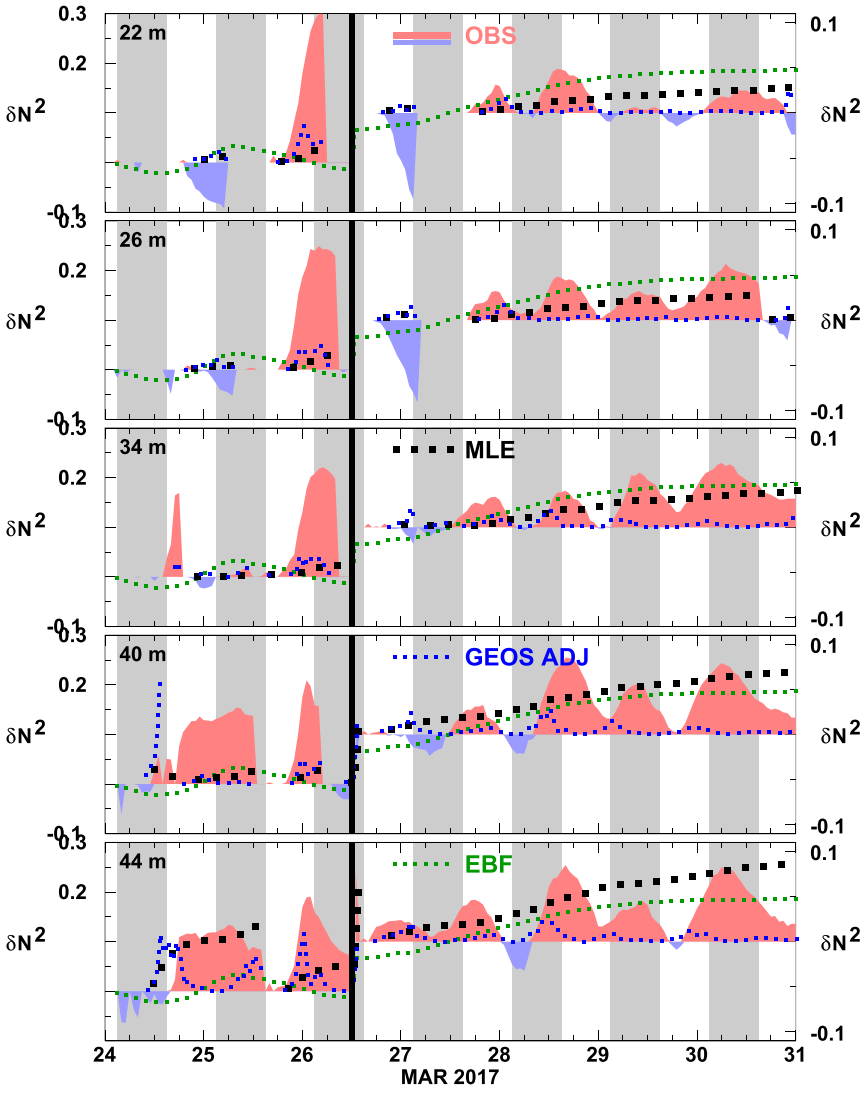

FIG. 15. Comparison of normalized measured advective restratification $\int(u_z b_x + v_z b_y)\,dt/N_0^2$ ($N_0 = 5 \times 10^{-3}$ rad s^{-1}) at 22–44-m depth (8) (which is in the remnant layer after 28 Mar) (OBS; pink and blue shading) with parameterizations based on (i) MLE instability $C_e H^2 \mu_{zz} \int b_h^2\,dt/f/N_0^2$ (10) (black dotted), (ii) geostrophic adjustment $(b_h^2/f^2)[1-\cos(ft')]/N_0^2$ (9) (GEOS; blue dotted), and (iii) bulk Ekman buoyancy flux (EBF) (13) (green dotted) assuming Ekman transport extends over the 55-m surface layer. Note that different vertical-axis scales amplify the signal after mid 26 Mar. Before 26 Mar, daytime measured advective restratification is stronger than any of the parameterizations (except 25 Mar at 44 m) and often destratifying because of storm-forced inertial shear. After 26 Mar, the subinertial envelope of measured advective restratification resembles MLE predictions while geostrophic adjustment is limited to oscillate between zero and b_h^2/f^2. Bulk EBF also resembles the subinertial envelope of the measured advective restratification but it is unlikely that Ekman fluxes penetrate into the insulated remnant layer.

almost its full ~55-m thickness every night followed by restratification to $N \sim 2 \times 10^{-3}$ rad s^{-1} during the day (Figs. 3 and 7). Starting on 28 March, destabilizing nocturnal surface buoyancy fluxes and wind stresses weaken while daytime stabilizing buoyancy fluxes remain strong (Figs. 7 and 8). A strongly stratified TL forms above ~20-m depth which is no longer eradicated at night starting on 30 March. Below the transition layer, an insulated RL restratifies for ~72 h.

The measurements are used to examine the roles of shortwave penetrative radiation, turbulent buoyancy fluxes and vertical shearing of horizontal buoyancy gradients in restratifying the surface layer on time scales from hours to days. Horizontal buoyancy gradients (b_x, b_y) are nearly depth-independent and

dominantly subinertial while vertical shears (u_z, v_z) inertial/diurnal (Figs. 5 and 10), arising from a combination of wind forcing and geostrophic adjustment.

Except on 26 March, buoyancy advective restratification (slumping) (8) is small (Figs. 11 and 12) and often destratifying despite unbalanced subinertial vertical shear and horizontal buoyancy gradients (Figs. 4–6) fulfilling a necessary condition for advective restratification $u_z b_x + v_z b_y$. This points to an HKE source for at least some of the shear advection, e.g., wind forcing. Prior to 28 March, daytime restratification of the surface layer can largely be accounted for by horizontal advection (26 March) and penetrative radiation (Figs. 11 and 12) with local turbulent buoyancy fluxes playing little role. Starting on 28 March, the restratification model (4) is not applicable above ~20-m depth because surface-forced convection influences the diurnal ML and stratified TL so that turbulent buoyancy fluxes cannot be determined with any fidelity from the χ_T measurements.

Isolated from nonlocal surface-forced mixing, the 22–46-m RL exhibits a sharp increase in stratification during 28 March, then continues to restratify through 31 March. Shortwave penetrative radiation $\int(\partial^2 J_b/\partial z^2)\,dt$ (6) and turbulence $\int(\partial^2\langle w'b'\rangle/\partial z^2)\,dt$ (7), both nonconservative 1D processes, are the dominant restratifying mechanisms (Figs. 11 and 12), so that potential vorticity will not be conserved. Horizontal advection $\int(u_z b_x + v_z b_y)\,dt$ (8) plays a weaker role.

Starting on 28 March, the sum $\sum\delta N^2$ (6)–(8) largely reproduces the measured ΔN^2 (5) between 22 and 46 m within the uncertainties of 15% (Fig. 12). Notable exceptions are transient underestimates at some depths and times (red stars in Fig. 12). Nocturnal peaks in ΔN^2 during these discrepancies arise from a small fraction (<20%) of float profiles. Shallower than 35 m, vertical density gradients are sharpened at the base of a homogenized overlying water column in these anomalous profiles, incoherent on lateral length scales < 0.5 km and temporal scales < 1 h (Fig. 13a). Deeper than 35 m, the discrepancies appear to be associated with subinertial uplift of the underlying pycnocline (Fig. 13b). Thus, the discrepancies arise because of infrequent transient exceptions to the assumption that remnant layer is not influenced by either (i) surface-forced convection from above or (ii) the pycnocline from below. These features do not appear to have any long-term impact here.

Advective restratification $\int(u_z b_x + v_z b_y)\,dt$ (8) exhibits inertial/diurnal fluctuations throughout the record (Fig. 14). Except during 24–26 March when there was intense buoyancy advective destratification in the lower half of the surface layer, it is almost depth-independent in contrast to the intensification at the top and bottom of the surface layer predicted by MLE (section 6; Boccaletti et al. 2007).

MLE predictions (10) are weaker than measured buoyancy advective restratification before 26 March (except 25 March at 44-m depth) (Fig. 15). After 28 March, the subinertial envelope of measured advective restratification resembles MLE predictions in the remnant layer. That the sum of penetrative radiation, turbulence and advective restratification $\sum\delta N^2$ reproduces the measured restratification ΔN^2 (Fig. 12)—with transient exceptions due to incursions of convective mixing from above and uplift of the pycnocline from below (Fig. 13)—suggests that that model (8) is able to close the stratification budget in the remnant layer.

While bulk Ekman buoyancy flux (12) is sometimes destratifying, it is not well-correlated with measured events in the early half of the record. Like MLE predictions, it resembles the subinertial envelope of measured advective restratification starting on 28 March. However, it is unlikely that Ekman fluxes penetrate below the transition layer.

To summarize the summary, restratification of the spring surface layer in the North Pacific Subtropical Front was primarily due to surface air–sea buoyancy fluxes, penetrative radiation, and turbulent buoyancy fluxes (Fig. 12). Vertical shearing of lateral buoyancy gradients plays a smaller role. Buoyancy advective restratification (8) resembles MLE parameterization predictions in the isolated remnant layer starting on 28 March that forms after nocturnal convection weakens and shoals (Fig. 15).

8. Discussion

Restratification by vertical shearing of lateral buoyancy gradients requires shear and buoyancy gradients that are out of thermal-wind balance (ageostrophic) as here (Fig. 6). Sufficiently strong nocturnal destratification resets all restratification processes as on 24–27 March and previously noted (e.g., Hosegood et al. 2008; Mahadevan et al. 2012; Haney et al. 2012). MLE restratification also competes with other spring restratification processes associated with increased solar radiation and weakening storms (e.g., Haney et al. 2012). In our measurements, buoyancy advective restratification (slumping) is limited to daytime before 28 March and the remnant layer starting on 28 March. It is weaker than shortwave penetrative radiation and turbulent buoyancy fluxes except on 26 March (Fig. 12).

Buoyancy advective restratification has previously been reported in the North Pacific Subtropical Front from a 33-h-long 15-km^2 survey time series (Hosegood et al. 2008) and in a stronger California Current front with $b_h \sim 10^{-6}\,\mathrm{s}^{-2} \sim 2fN$ in a 30-h time series (Johnson et al. 2020a). Johnson et al. also reported turbulence dissipation rates of $\sim 10^{-6}\,\mathrm{W\,kg}^{-1}$ comparable to those found here and large vertical velocities in contrast to predictions from the omega equation. Because of their short durations and storm forcing, the Hosegood et al. (2008) and Johnson et al. (2020a) results may be most analogous to our transient 26 March advective restratification event (Fig. 12) where storm-driven inertial shear is likely responsible (Fig. 15).

Buoyancy advective restratification making little contribution in the spring North Pacific Subtropical Front (Figs. 11 and 12) is consistent with predictions for this region based on a global comparison of the 1D Price et al. (1986) model to Argo float profiles (Johnson et al. 2016). Measured horizontal buoyancy gradients were similar to those reported by Mahadevan et al. (2012) south of Iceland where inferred advective restratification, equivalent to ageostrophic velocity differences in excess of $10\,\mathrm{cm\,s}^{-1}$ over the 200-m surface boundary layer persisting over 10 days and 250 km, was reported prior to

dominance by spring shortwave penetrative radiation. In contrast, the EM float measurements here recorded a 7-day average velocity difference across 50-m depth of $\sim 0.3\ \mathrm{cm\ s^{-1}}$ (Figs. 6a,b) and find only a small advective contribution to restratification. This may be because our thinner surface layer implies a greater influence of penetrative radiation. Additionally, the difference may be because of relative timing of (i) spring penetrative radiation (Follows and Dutkiewicz 2002), (ii) weather-related storms, (iii) the lateral buoyancy gradient in the North Pacific Subtropical Front being less extensive than that in the North Atlantic Current so that there is less lateral APE, or (iv) the 72-h interval after the last nocturnal destratification in our data simply not being long enough for mixed-layer eddy instabilities to grow significantly given mixed-layer $\sim O(10)$-day instability time scales (1). In support of (iv), numerical simulations find that restratification of surface-layer fronts is controlled by vertical processes at day 3, with MLE advective restratification only dominating after day 6 (Haine and Marshall 1998; Haney et al. 2012).

Destratifying shear advection events (Figs. 14 and 15) cannot be reproduced by either geostrophic adjustment (9) or MLE instability (10) because horizontal buoyancy-gradient APE is their sole energy source. Neither parameterization takes into account HKE from (i) Ekman shear or inertial oscillations which will accompany wind-forced homogenization of the surface layer, nor (ii) the submesoscale frontal jets that will be vertically homogenized along with buoyancy. Sources of surface-layer velocity other than geostrophic adjustment (Tandon and Garrett 1994, 1995) and mixed-layer eddy instability (Samelson and Chapman 1995; Young and Chen 1995; Haine and Marshall 1998; Boccaletti et al. 2007) cannot be neglected in submesoscale buoyancy advective restratification where HKE is comparable to or larger than APE. Tandon and Garrett (1995) included vertically homogenized frontal jets but under the assumption that $(NH/fL)^2 \ll 1$ which also implies HKE/APE $\ll 1$, not representative of our measurements or the submesoscale in general.

Inertial/diurnal shears $\sim O(N)$ dominate over subinertial shears $\sim O(0.2N)$ in the surface layer (Fig. 4) so must be taken into account for daytime advective restratification events (Figs. 11–15). Independent of geostrophic adjustment, $\sim O(N)$ inertial shear is ubiquitous. Preexisting or simultaneously forced inertial shear from wind (Pollard and Millard 1970; Plueddemann and Farrar 2006) might be in or out of phase (Crawford and Large 1996) with shear generated by geostrophic adjustment or MLE instability, so could act either to restratify or destratify. By acting to strengthen or weaken daytime restratification, they may have a rectified impact on spring phytoplankton bloom timing by heterogeneously amplifying stratification and primary production during daylight hours, and preconditioning the surface layer for more permanent shoaling, thus contributing to patchiness in surface-layer stratification and primary productivity even within strong buoyancy fronts (Dutkiewicz et al. 2001).

The fieldwork described here emphasizes the challenges in characterizing the role of advection in spring restratification of the surface boundary layer. As well as being localized to buoyancy fronts and a short interval during spring, additional heterogeneity is imposed by the timing of spring storms, weather-dependent penetrative radiation and surface-layer convection, including nonlocal surface-forced convective mixing on unresolved lateral scales less than 0.5 km and temporal scales less than 1 h (Fig. 13), making dominance by buoyancy advective restratification (slumping) difficult to capture. Many more measurements, both at other more favorable locations (Johnson et al. 2016) and of durations exceeding 10 days to resolve MLE instability (Haine and Marshall 1998; Haney et al. 2012; Mahadevan et al. 2012), are needed to establish how, when, and where the competing contributions of radiation, meteorology, wind-driven inertial shear, geostrophic adjustment, Ekman buoyancy flux, and MLE instability contribute to the surface-layer stratification budget, timing of spring mixed-layer shoaling and phytoplankton blooms. While localized transient events (Figs. 12 and 13) did not appear to have any long-term impact here, it is uncertain if this will always be the case.

Acknowledgments. This work would not have been possible without the expert instrument preparation by engineers Avery Snyder, Ryan Newell, Chris Siani, Sam Fletcher, and Eric Boget, as well as the vigilance of volunteer watchstanders Rosalind Echols, Hyang Yoon, Olga Mironenko, Keaton Snyder, and Ethan Brush, and the captain and crew of the R/V *Sikuliaq*. The manuscript benefited from feedback from Leah Johnson, Carter Ohlmann, Baylor Fox-Kemper, Tom Farrar, and two anonymous reviewers. This research was made possible by NSF Grants OCE-1536681 and OCE-1536314. In tribute to Thomas B. Sanford whose instrumental innovations made this work possible.

Data availability statement. Site 3 EM-APEX float profile and processed data files used for this research can be found at http://hdl.handle.net/1773/46925.

REFERENCES

Behrenfeld, M., 2010: Abandoning Sverdrup's critical depth hypothesis on phytoplankton blooms. *Ecology*, **91**, 977–989, https://doi.org/10.1890/09-1207.1.

Belcher, S. E., and Coauthors, 2012: A global perspective on Langmuir turbulence in the ocean surface boundary layer. *Geophys. Res. Lett.*, **39**, L18605, https://doi.org/10.1029/2012GL052932.

Boccaletti, G., R. Ferrari, and B. Fox-Kemper, 2007: Mixed layer instabilities and restratification. *J. Phys. Oceanogr.*, **37**, 2228–2250, https://doi.org/10.1175/JPO3101.1.

Brainerd, K. E., and M. C. Gregg, 1993a: Diurnal restratification and turbulence in the oceanic surface mixed layer: 1. Observations. *J. Geophys. Res.*, **98**, 22 645–22 656, https://doi.org/10.1029/93JC02297.

——, and ——, 1993b: Diurnal restratification and turbulence in the oceanic surface mixed layer: 2. Modeling. *J. Geophys. Res.*, **98**, 22 657–22 664, https://doi.org/10.1029/93JC02298.

Capet, X., E. J. Campos, and A. M. Paiva, 2008: Submesoscale activity over the Argentinian shelf. *Geophys. Res. Lett.*, **35**, L15605, https://doi.org/10.1029/2008GL034736.

Carlson, J. A., J. H. Dunlap, J. B. Girton and T. B. Sanford, 2006: EM-APEX operator's manual. APL-UW Tech. Rep., 48 pp.,

http://www.cmar.csiro.au/argo/dmqc/html/Float_manuals/EM-APEX_manual_fin.pdf.

Crawford, G. B., and W. G. Large, 1996: A numerical investigation of resonant inertial response of the ocean to wind forcing. *J. Phys. Oceanogr.*, **26**, 873–891, https://doi.org/10.1175/1520-0485(1996)026<0873:ANIORI>2.0.CO;2.

Cushman-Roisin, B., 1984: On the maintenance of the Subtropical Front and its associated countercurrent. *J. Phys. Oceanogr.*, **14**, 1179–1190, https://doi.org/10.1175/1520-0485(1984)014<1179:OTMOTS>2.0.CO;2.

Dauhajre, D. P., and J. C. McWilliams, 2018: Diurnal evolution of submesoscale front and filament circulations. *J. Phys. Oceanogr.*, **48**, 2343–2361, https://doi.org/10.1175/JPO-D-18-0143.1.

de Boyer Montégut, C., G. Madec, A. S. Fischer, A. Lazar, and D. Iudicone, 2004: Mixed layer depth over the global ocean: An examination of profile data and a profile-based climatology. *J. Geophys. Res.*, **109**, C12003, https://doi.org/10.1029/2004JC002378.

Dutkiewicz, S., M. Follows, J. Marshall, and W. Gregg, 2001: Interannual variability of phytoplankton abundances in the North Atlantic. *Deep-Sea Res. II*, **48**, 2323–2344, https://doi.org/10.1016/S0967-0645(00)00178-8.

Follows, M., and S. Dutkiewicz, 2002: Meteorological modulation of the North Atlantic spring bloom. *Deep-Sea Res. II*, **49**, 321–344, https://doi.org/10.1016/S0967-0645(01)00105-9.

Fox-Kemper, B., and R. Ferrari, 2008: Parameterization of mixed layer eddies. 2: Prognosis and impact. *J. Phys. Oceanogr.*, **38**, 1166–1179, https://doi.org/10.1175/2007JPO3788.1.

——, ——, and R. Hallberg, 2008: Parameterization of mixed layer eddies. Part 1: Theory and diagnosis. *J. Phys. Oceanogr.*, **38**, 1145–1165, https://doi.org/10.1175/2007JPO3792.1.

——, and Coauthors, 2011: Parameterization of mixed layer eddies. 3: Implementation and impact on global ocean climate simulations. *Ocean Modell.*, **39**, 61–78, https://doi.org/10.1016/j.ocemod.2010.09.002.

Gregg, M. C., E. A. D'Asaro, J. J. Riley, and E. Kunze, 2018: Mixing efficiency in the ocean. *Annu. Rev. Mar. Sci.*, **10**, 443–473, https://doi.org/10.1146/annurev-marine-121916-063643.

Haine, T. W. N., and J. Marshall, 1998: Gravitational, symmetric, and baroclinic instability of the ocean mixed layer. *J. Phys. Oceanogr.*, **28**, 634–658, https://doi.org/10.1175/1520-0485(1998)028<0634:GSABIO>2.0.CO;2.

Haney, S., and Coauthors, 2012: Hurricane restratification rates of one-, two- and three-dimensional processes. *J. Mar. Res.*, **70**, 824–850, https://doi.org/10.1357/002224012806770937.

Hosegood, P., M. C. Gregg, and M. H. Alford, 2006: Submesoscale lateral density structure in the oceanic surface mixed layer. *Geophys. Res. Lett.*, **33**, L22604, https://doi.org/10.1029/2006GL026797.

——, ——, and ——, 2008: Restratification of the surface mixed layer with submesoscale lateral density gradients: Diagnosing the importance of the horizontal dimension. *J. Phys. Oceanogr.*, **38**, 2438–2460, https://doi.org/10.1175/2008JPO3843.1.

——, ——, and ——, 2013: Wind-driven submesoscale subduction in the North Pacific Subtropical Front. *J. Geophys. Res. Oceans*, **118**, 5333–5352, https://doi.org/10.1002/jgrc.20385.

Hsu, J.-Y., R.-C. Lien, E. A. D'Asaro, and T. B. Sanford, 2018: Estimates of surface waves using subsurface EM-APEX floats under Typhoon Fanapi 2010. *J. Ocean. Atmos. Tech*, **35**, 1053–1075, https://doi.org/10.1175/JTECH-D-17-0121.1.

Huisman, J., P. van Oostveen, and F. Weissing, 1999: Critical depth and critical turbulence: Two different mechanisms for the development of phytoplankton blooms. *Limnol. Oceanogr.*, **44**, 1781–1787, https://doi.org/10.4319/lo.1999.44.7.1781.

Ineichen, P., and R. Perez, 2002: A new airmass-independent formulation for the Linke turbidity coefficient. *Sol. Energy*, **73**, 151–157, https://doi.org/10.1016/S0038-092X(02)00045-2.

Jochum, M., 2009: Impact of latitudinal variations in vertical diffusivity on climate simulations. *J. Geophys. Res.*, **114**, C01010, https://doi.org/10.1029/2008JC005030.

Johnson, G. C., S. Schmidtko, and J. M. Lyman, 2012: Relative contributions of temperature and salinity to seasonal mixed layer density changes and horizontal density gradients. *J. Geophys. Res.*, **117**, C04015, https://doi.org/10.1029/2011JC007651.

Johnson, L., C. N. Lee, and E. A. D'Asaro, 2016: Global estimates of lateral springtime restratification. *J. Phys. Oceanogr.*, **46**, 1555–1573, https://doi.org/10.1175/JPO-D-15-0163.1.

——, C. M. Lee, E. A. D'Asaro, L. Thomas, and A. Shcherbina, 2020a: Restratification at a California Current upwelling front. Part I: Observations. *J. Phys. Oceanogr.*, **50**, 1455–1472, https://doi.org/10.1175/JPO-D-19-0203.1.

——, ——, ——, J. O. Wenegrat, and L. N. Thomas, 2020b: Restratification at a California Current upwelling front. Part II: Dynamics. *J. Phys. Oceanogr.*, **50**, 1473–1487, https://doi.org/10.1175/JPO-D-19-0204.1.

Kantha, L. H., and C. A. Clayson, 1994: An improved mixed layer model for geophysical applications. *J. Geophys. Res.*, **99**, 25 235–25 266, https://doi.org/10.1029/94JC02257.

Klymak, J. M., and M. C. Gregg, 2001: Three-dimensional nature of flow near a sill. *J. Geophys. Res.*, **106**, 22 295–22 311, https://doi.org/10.1029/2001JC000933.

Kraus, E. B., and J. S. Turner, 1967: A one-dimensional model of the seasonal thermocline 2. The general theory and its consequences. *Tellus*, **19A**, 98–106, https://doi.org/10.1111/j.2153-3490.1967.tb01462.x.

Large, W. F., J. C. McWilliams, and S. C. Doney, 1994: Oceanic vertical mixing: A review and a model with a nonlocal boundary layer parameterization. *Rev. Geophys.*, **32**, 363–403, https://doi.org/10.1029/94RG01872.

Longhurst, A., and W. Harrison, 1989: The biological pump: Profiles of plankton production and consumption in the upper ocean. *Prog. Oceanogr.*, **22**, 47–123, https://doi.org/10.1016/0079-6611(89)90010-4.

——, S. Sathyendranath, T. Platt, and C. Caverhill, 1995: An estimate of global primary production in the ocean from satellite radiometer data. *J. Plankton Res.*, **17**, 1245–1271, https://doi.org/10.1093/plankt/17.6.1245.

MacWhorter, M. A., and R. A. Weller, 1991: Error in measurements of incoming shortwave radiation made from ships and buoys. *J. Atmos. Oceanic Technol.*, **8**, 108–117, https://doi.org/10.1175/1520-0426(1991)008<0108:EIMOIS>2.0.CO;2.

Mahadevan, A., A. Tandon, and R. Ferrari, 2010: Rapid changes in mixed-layer stratification driven by submesoscale instabilities and winds. *J. Geophys. Res.*, **115**, C03017, https://doi.org/10.1029/2008JC005203.

——, E. A. D'Asaro, C. M. Lee, and M. J. Perry, 2012: Eddy-driven stratification initiates North Atlantic spring phytoplankton blooms. *Science*, **337**, 54–58, https://doi.org/10.1126/science.1218740.

McGillicuddy, D. J., and Coauthors, 2007: Eddy/wind interactions stimulate extraordinary mid-ocean plankton blooms. *Science*, **316**, 1021–1026, https://doi.org/10.1126/science.1136256.

Morel, A., and R. C. Smith, 1974: Relation between total quanta and total energy for aquatic photosynthesis. *Limnol. Oceanogr.*, **19**, 591–600, https://doi.org/10.4319/lo.1974.19.4.0591.

Niiler, P. P., and E. B. Kraus, 1977: One-dimensional models of the upper ocean. *Modelling and Prediction of the Upper Layers of the Ocean*, E. B. Kraus, Ed., Pergamon Press, 143–172.

Ohlmann, J. C., 2003: Ocean radiant heating in climate models. *J. Climate*, **16**, 1337–1351, https://doi.org/10.1175/1520-0442-16.9.1337.

——, and D. A. Siegel, 2000: Ocean radiant heating. Part II: Parameterizing solar radiation transmission through the upper ocean. *J. Phys. Oceanogr.*, **30**, 1849–1865, https://doi.org/10.1175/1520-0485(2000)030<1849:ORHPIP>2.0.CO;2.

Osborn, T. R., 1980: Estimates of the local rate of vertical diffusion from dissipation measurements. *J. Phys. Oceanogr.*, **10**, 83–89, https://doi.org/10.1175/1520-0485(1980)010<0083:EOTLRO>2.0.CO;2.

——, and C. S. Cox, 1972: Oceanic fine structure. *Geophys. Fluid Mech*, **3**, 321–345, https://doi.org/10.1080/03091927208236085.

Paulson, C. A., and J. J. Simpson, 1977: Irradiance measurements in the upper ocean. *J. Phys. Oceanogr.*, **7**, 952–956, https://doi.org/10.1175/1520-0485(1977)007<0952:IMITUO>2.0.CO;2.

Plueddemann, A. J., and J. T. Farrar, 2006: Observations and models of the energy flux from the wind to mixed-layer inertial currents. *Deep-Sea Res. II*, **53**, 5–30, https://doi.org/10.1016/j.dsr2.2005.10.017.

Pollard, R., and R. Millard, 1970: Comparison between observed and simulated wind-generated inertial oscillations. *Deep-Sea Res. Oceanogr. Abstr.*, **17**, 813–821, https://doi.org/10.1016/0011-7471(70)90043-4.

Price, J. F., R. A. Weller, and R. Pinkel, 1986: Diurnal cycling: Observations and models of the upper-ocean response to diurnal heating, cooling, and wind mixing. *J. Geophys. Res.*, **91**, 8411–8427, https://doi.org/10.1029/JC091iC07p08411.

——, ——, C. M. Bowers, and M. G. Briscoe, 1987: Diurnal response of sea surface temperature observed at the Long-Term Upper Ocean Study (34°N, 70°W) in the Sargasso Sea. *J. Geophys. Res.*, **92**, 14 480–14 490, https://doi.org/10.1029/JC092iC13p14480.

Roden, G. I., 1975: On North Pacific temperature, salinity, sound velocity and density fronts and their relation to the wind and energy flux fields. *J. Phys. Oceanogr.*, **5**, 557–571, https://doi.org/10.1175/1520-0485(1975)005<0557:ONPTSS>2.0.CO;2.

Rodex, G. I., 1981: Mesoscale thermohaline, sound velocity and baroclinic flow structure of the Pacific Subtropical Front during winter of 1980. *J. Phys. Oceanogr.*, **11**, 658–675, https://doi.org/10.1175/1520-0485(1981)011<0658:MTSVAB>2.0.CO;2.

Rudnick, D. L., and R. Ferrari, 1999: Compensation of horizontal temperature and salinity gradients in the ocean mixed layer. *Science*, **283**, 526–529, https://doi.org/10.1126/science.283.5401.526.

Sabine, C. L., and Coauthors, 2004: The oceanic sink for anthropogenic CO_2. *Science*, **305**, 367–371, https://doi.org/10.1126/science.1097403.

Samelson, R. M., and D. C. Chapman, 1995: Evolution of the instability of a mixed-layer front. *J. Geophys. Res.*, **100**, 6743–6759, https://doi.org/10.1029/94JC03216.

Sanford, T. B., J. A. Carlson, J. H. Dunlap, D. C. Webb, and J. B. Girton, 2005: Autonomous velocity and density profiler: EM-APEX. *Proc. IEEE/OES Eighth Working Conf. on Current Measurement Technology*, Southampton, United Kingdom, Institute of Electrical and Electronics Engineers, 152–156.

——, J. F. Price, and J. B. Girton, 2011: Upper-ocean response to Hurricane Frances (2004) observed by profiling EM-APEX floats. *J. Phys. Oceanogr.*, **41**, 1041–1056, https://doi.org/10.1175/2010JPO4313.1.

Shay, T. J., and M. C. Gregg, 1986: Convectively driven turbulent mixing in the upper ocean. *J. Phys. Oceanogr.*, **16**, 1777–1798, https://doi.org/10.1175/1520-0485(1986)016<1777:CDTMIT>2.0.CO;2.

Shcherbina, A. Y., M. C. Gregg, M. H. Alford, and R. R. Harcourt, 2009: Characterizing thermohaline intrusions in the North Pacific Subtropical Frontal zone. *J. Phys. Oceanogr.*, **39**, 2735–2756, https://doi.org/10.1175/2009JPO4190.1.

——, ——, ——, and ——, 2010: Three-dimensional structure and temporal evolution of submesoscale thermohaline intrusions in the North Pacific Subtropical Frontal zone. *J. Phys. Oceanogr.*, **40**, 1669–1689, https://doi.org/10.1175/2010JPO4373.1.

Smetacek, V., K. Bröckel, B. Zeitzschel, and W. Zenk, 1978: Sedimentation of particulate matter during a phytoplankton spring bloom in relation to the hydrographical regime. *Mar. Biol.*, **47**, 211–226, https://doi.org/10.1007/BF00541000.

Stone, P. H., 1970: On non-geostrophic baroclinic stability: Part 2. *J. Atmos. Sci.*, **27**, 721–726, https://doi.org/10.1175/1520-0469(1970)027<0721:ONGBSP>2.0.CO;2.

Stramma, L., P. Cornillon, R. A. Weller, J. F. Price, and M. G. Briscoe, 1986: Large diurnal sea surface temperature variability: Satellite and in situ measurements. *J. Phys. Oceanogr.*, **16**, 827–837, https://doi.org/10.1175/1520-0485(1986)016<0827:LDSSTV>2.0.CO;2.

Sutherland, G., G. Reverdin, L. Marie, and B. Ward, 2014: Mixed and mixing layer depths in the ocean surface boundary layer under conditions of diurnal stratification. *Geophys. Res. Lett.*, **41**, 8469–8476, https://doi.org/10.1002/2014GL061939.

Sverdrup, H., 1953: On conditions for vernal blooming of phytoplankton. *Cons. Int. Explor. Mer.*, **18**, 287–295, https://doi.org/10.1093/icesjms/18.3.287.

Swart, S., S. J. Thomalla, and P. M. S. Montiero, 2015: The seasonal cycle of mixed layer dynamics and phytoplankton biomass in the Sub-Antarctic Zone: A high-resolution glider experiment. *J. Mar. Syst.*, **147**, 103–115, https://doi.org/10.1016/j.jmarsys.2014.06.002.

Tandon, A., and C. Garrett, 1994: Mixed layer restratification due to a horizontal density gradient. *J. Phys. Oceanogr.*, **24**, 1419–1424, https://doi.org/10.1175/1520-0485(1994)024<1419:MLRDTA>2.0.CO;2.

——, and ——, 1995: Geostrophic adjustment and restratification of a mixed layer with horizontal gradients above a stratified layer. *J. Phys. Oceanogr.*, **25**, 2229–2241, https://doi.org/10.1175/1520-0485(1995)025<2229:GAAROA>2.0.CO;2.

Taylor, J. R., and R. Ferrari, 2010: Buoyancy and wind-driven convection at mixed layer density fronts. *J. Phys. Oceanogr.*, **40**, 1222–1242, https://doi.org/10.1175/2010JPO4365.1.

——, and ——, 2011: Ocean fronts trigger high-latitude phytoplankton blooms. *Geophys. Res. Lett.*, **38**, L23601, https://doi.org/10.1029/2011GL049312.

Thomas, L. N., and C. M. Lee, 2005: Intensification of ocean fronts by downfront winds. *J. Phys. Oceanogr.*, **35**, 1086–1102, https://doi.org/10.1175/JPO2737.1.

——, J. R. Taylor, R. Ferrari, and T. M. Joyce, 2013: Symmetric instability in the Gulf Stream. *Deep-Sea Res. II*, **91**, 96–110, https://doi.org/10.1016/j.dsr2.2013.02.025.

Townsend, D., L. Cammen, P. Holligan, D. Campbell, and N. Pettigrew, 1994: Causes and consequences of variability in the timing of spring phytoplankton blooms. *Deep-Sea Res. I*, **41**, 747–765, https://doi.org/10.1016/0967-0637(94)90075-2.

Van Woert, M., 1982: The Subtropical Front: Satellite observations during FRONTS '80. *J. Geophys. Res.*, **87**, 9523–9536, https://doi.org/10.1029/JC087iC12p09523.

Young, W. R., and L. G. Chen, 1995: Baroclinic instability and thermohaline gradient alignment in the mixed layer. *J. Phys. Oceanogr.*, **25**, 3172–3185, https://doi.org/10.1175/1520-0485(1995)025<3172:BIATGA>2.0.CO;2.